Shear-Enhanced Gradient Inelastic Force-Based Frame Element Formulation for Analysis of Shear-critical Reinforced Concrete Members

M. Aghajani Delavar[(1)], M. Salehi[(2)], P. Sideris[(3)]

[(1)] *Graduate Student Researcher, Zachry Department of Civil and Environmental Engineering, Texas A&M University, aghajani.mo@tamu.edu*

[(2)] *Project Consultant, Simpson Gumpertz & Heger, msalehi@sgh.com*

[(3)] *Associate Professor, Zachry Department of Civil and Environmental Engineering, Texas A&M University, petros.sideris@tamu.edu*

Abstract

A large number of structures in the U.S. and worldwide include non-ductile reinforced concrete (RC) frames with columns and beams that are prone to shear failure. Due to the brittle nature of shear failures, accurate simulation of RC structures with shear-critical members is essential to predicting their overall capacity under severe loading scenarios (e.g. earthquakes) and designing effective retrofits and upgrades. In this paper, a previously developed gradient inelastic (GI) force-based (FB) beam-column element formulation capable of capturing axial-flexural interaction and predicting flexural failures is extended to account for axial-flexural-shear interactions in RC members in order to predict shear failures. The proposed *shear-enhanced* GI FB element formulation advances the original GI FB element formulation by developing higher-order cross-section kinematics, i.e., beyond the plane sections assumption, and by developing a 3D concrete constitutive model. The higher-order cross-section kinematics can simulate strain distribution of the cross-section more accurately, while using 3D concrete constitutive models at the element's cross-sections permit simulation of axial-flexural-shear interactions. To incorporate the confinement effects of transverse steel reinforcement, through-the-depth stress equilibrium is strictly enforced in the transverse directions of the member's cross-section. To eliminate strain localization phenomena, new gradient nonlocality relationships are introduced, in addition to those of the original GI FB formulation. The proposed element formulation is implemented in the OpenSees structural analysis software and is shown to maintain continuous macroscopic section strain distributions over the element length during softening and discretization convergent responses, thereby eliminating the strain

localization phenomena. In addition, the predictions of the shear-enhanced GI FB element formulation are compared with data available from experiments on RC beams and columns.

Keywords: *reinforced concrete, beam element, strain localization, gradient inelastic element, axial-shear-flexural interaction, shear critical*

1. Introduction

Reinforced concrete (RC) structures are usually subjected to a variety of loading conditions that simultaneously generate flexural, shear and axial internal loads in their members, resulting in triaxial stress/strain states. RC members are nowadays designed to fail in a ductile manner in flexure, but members with small span-to-depth ratios or those designed using outdated codes can suffer from brittle failures, such as shear or flexure-shear failures. Therefore, accurate numerical simulation of axial-flexural-shear interactions in RC members is crucial to accurately evaluating the performance of such members under extreme loading scenarios.

Two approaches are generally adopted for efficient finite element modeling of RC members: (*i*) using elastic beam-column elements with concentrated plasticity at their ends (Kunnath et al. 1990; Ricles et al. 1998; Lee et al. 2009; Xu and Zhang 2011; Roh et al. 2012; LeBorgne and Ghannoum 2014), and (*ii*) using distributed-plasticity beam-column elements (Filippou et al. 1992; Mergos and Kappos 2008; Sezen and Chowdhury 2009; Mergos and Beyer 2014). Because of its superior computational efficiency, the former approach is vastly employed in the literature (Haselton 2007; Haselton et al. 2016; Aghajani Delavar and Bargi 2018; Aghajani Delavar and Bargi 2020Hellesland and Scordelis 1981; Spacone et al. 1996; Neuenhofer and Filippou 1997); however, it cannot predict spread of damage/plasticity and relies on calibrations based on component/member testing. Despite their higher computational cost, distributed-plasticity beam-column elements can predict the spread of damage/plasticity along the modeled beams/columns by using several integration points (IPs) representing nonlinear cross section responses along their lengths. Because those IPs are usually represented via fiber sections, distributed-plasticity beam-column elements are also known as fiber elements. Two major groups of fiber element formulations have been developed, namely, stiffness/displacement-based (DB) and flexibility/force-based (FB). DB formulations employ predefined displacement interpolation functions along their lengths and satisfy the force equilibrium only in an average sense (through the virtual work method) (Priestley 1997; Limkatanyu and Spacone 2002). Contrarily, FB formulations strictly satisfy force equilibrium, making them capable of capturing the section strain/curvature distributions over the element lengths more accurately. However, in the presence of softening, conventional FB formulations lead to unrealistic strain singularities that are manifested as strain localization and result in secondary problems, such as lack of response objectivity and numerical instability (Zeris and Mahin 1988; Coleman and Spacone 2001; Sideris 2012; Sideris and Salehi 2016). To eliminate the strain localization phenomenon, several methods have been proposed that introduce a

characteristic length into either the material constitutive models or the element formulation, including constitutive law re-scaling (Coleman and Spacone 2001), plastic hinge integration methods (Scott and Fenves 2006; Scott and Hamutçuoğlu 2008; Almeida et al. 2012), nonlocal models (Khaloo and Tariverdilo 2002; Valipour and Foster 2009, Feng et al. 2016; Nikoukalam and Sideris 2019), and gradient models (Sideris and Salehi 2016; Salehi and Sideris 2017; Salehi and Sideris 2018).

Fiber beam-column element formulations have commonly focused on flexural responses as they are based on the Euler-Bernoulli (EB) beam theory (e.g., Feng et al. 2019) and do not explicitly consider shear effects. The majority of fiber element formulations for shear critical elements are based on the Timoshenko beam theory (e.g., Filippou and Saritas 2006; Feng and Ren 2021), which accounts for shear behavior in an average sense by assuming a linear variation of transverse displacement of the cross-section, which results in a uniform shear strain profile over the cross-section. In the case of linear elastic beams, and in order to avoid the beam prediction errors due to the uniform strain profile assumption, correction factors are applied to the shear stiffness coefficients of the respective member stiffness matrices (e.g., Mindlin and Deresiewicz 1953; Cowper 1966; Kaneko 1975; Jensen 1983). However, no such correction factors are available for inelastic beams. Beam theories with higher-order cross-section kinematics have been shown to reproduce more accurate strain profiles due to nonlinear variation of the deformation fields of the cross-section. Popular higher-order beam theories include (Zia and Khan 2018) the third-order beam theory, the trigonometric shear deformation beam theory, the hyperbolic shear deformation beam theory, and the exponential shear deformation beam theory. In these theories, the additional parameters introduced by the higher-order cross-section kinematics are determined by enforcing zero shear stress conditions at the boundaries of the cross-section under the assumption of linear elastic material response.

Most available flexural-shear fiber beam element formulations follow two main approaches: (*a*) incorporating axial-flexural-shear interaction at the element level by inserting shear springs at the element ends (e.g., D'Ambrisi and Filippou 1999; Marini and Spacone 2006; Mergos and Kappos 2008; Xu and Zhang 2011; Lodhi and Sezen 2012; Xu and Zhang 2012), and (*b*) considering shear deformation at the cross-section by adopting Timoshenko or higher-order beam theories rather than EB beam theory (e.g., Petrangeli et al. 1999; Bairan and Mari 2007; Ceresa et al. 2007; Ceresa et al. 2009; Saritas and Filippou 2009; Mohr et al. 2010; Mullapudi and Ayoub 2012; Stramandinoli and La Rovere 2012; Correia et al. 2015; Li et al. 2016). In the second approach, which is more straightforward, the accuracy and efficiency of

the element mainly relies on the selection of multiaxial concrete models. Commonly used models are the microplane models (e.g., Petrangeli et al. 1999; Jiang and Kurama 2010), smeared crack models (e.g. Vecchio and Collins 1988; Bentz 2000; Remino and Trento 2004; Garcia and Bernat 2006; Rajapakse et al. 2019; Hippola et al. 2022) and damage plasticity models (e.g., Ju 1989; Lee and Fenves 1998; Wu et al. 2006; Mullapudi and Ayoub 2012; Feng et al. 2019). Some research studies have also focused on integrating combined shear and torsional effects within frame elements (e.g., Saadé et al. 2004; Garcia and Bernat 2006; Garcia and Mari 2006; Kagermanov and Ceresa 2018; Nguyen et al. 2019). While higher-order cross-section kinematics have been employed in some DB formulations investigating shear failures (e.g., Garcia and Bernat 2006; Garcia and Mari 2006), use of higher-order cross-section kinematics in FB element formulations intending to capture axial-flexural-shear interaction remain limited (Mohr et al. 2010; Correia et al. 2015; Di Re et al. 2018).

In the presence of material models with softening branches, conventional FB formulations (and simulations of members with series of DB elements) suffer from strain localizations and loss of response objectivity. While strain localization phenomena have been more extensively studied for flexure-critical elements (Khaloo and Tariverdilo 2002; Valipour and Foster 2009; Sideris and Salehi 2016; Salehi and Sideris 2017; Kenawy et al. 2018; Kenawy et al. 2020), similar studies are fairly limited for shear-critical elements and for flexure-shear-critical elements (Feng et al. 2019; Feng and Ren 2021). In more recent years, the majority of studies addressing flexural softening have focused on incorporating concepts from nonlocal and gradient mechanics (Khaloo and Tariverdilo 2002; Valipour and Foster 2009; Sideris and Salehi 2016; Salehi and Sideris 2017; Kenawy et al. 2018; Kenawy et al. 2020). As part of these studies, the gradient inelastic (GI) beam theory together with a flexibility-based element formulation were recently proposed by Sideris and Salehi (2016) and Salehi and Sideris (2017), and were later extended to incorporate finite strains (Salehi and Sideris 2018). A major advantage of the GI FB beam element formulation is its capability to integrate any type of uniaxial material model, such as elastic, plastic, hardening, softening, and combinations of those because its gradient nonlocality relations are decoupled from the constitutive laws (Salehi and Sideris 2017). Such advantages have allowed the use of this element formulation in the collapse analysis of RC building and bridge structures (Salehi et al. 2017; 2020). In the original GI FB element formulation, the “plane sections” assumption results in uniform shear strain distribution over the cross-section, and the shear response is decoupled

from the normal stress/strain response. Herein, the GI element formulation is extended to capture shear failures and axial-flexural-shear interactions in RC members.

2. Scope and Innovations

This paper extends the original GI beam theory and the corresponding GI flexibility-based beam-column element formulation, which is capable of capturing axial-flexural interactions and predicting flexural failures, to account for axial-flexural-shear interactions and predict shear failures in RC members, while simultaneously achieving *response objectivity*. This is achieved by incorporating (*i*) higher-order cross-section kinematics to describe higher-order deformation profiles, (*ii*) cross-sectional through-the-depth equilibrium to predict normal strain distributions in the transverse directions and to compensate for confinement effects, and (*iii*) 3D concrete constitutive relations to simulate triaxial stress/strain interactions. The adopted 3D concrete constitutive relations are based on the plastic-damage model of Lee and Fenves (1998), which, amongst other modifications, it is also modified to include the effect of compression softening due to the presence of reinforcement. The higher-order cross-section kinematics are determined through satisfaction of cross-section boundary conditions (BCs) and do not introduce additional element degrees of freedom. To eliminate strain localization phenomena, new gradient nonlocality relationships are introduced, in addition to those of the original GI FB formulation. The resulting *shear-enhanced* GI element formulation is implemented in the structural analysis software OpenSees and is shown to eliminate strain localization phenomena during softening, thus, providing mesh-convergent (objective) responses. Additionally, the predictions of the shear-enhanced GI element formulation are compared with available experimental data from a number of tests on RC columns and beams.

3. Cross-section Kinematics

In order to capture shear effects, the following 3rd order cross-section kinematics (in 3D) with six degrees of freedom, which result from those proposed by Levinson (1981) in 2D, are adopted herein:

$$\begin{cases} u(x,y,z) = u_o(x) - y\theta_z(x) + z\theta_y(x) - y^3\psi_z(x) + z^3\psi_y(x) \\ v(x,y,z) = v_o(x) - z\theta_x(x) + z\psi_x(x) \\ w(x,y,z) = w_o(x) + y\theta_x(x) + y\psi_x(x) \end{cases} \quad (1)$$

In the above equations, $u(x,y,z)$, $v(x,y,z)$ and $w(x,y,z)$ are the displacements of a point at the reference coordinates (x,y,z) in x, y, and z directions, respectively; $u_o(x)$, $v_o(x)$ and $w_o(x)$ are the displacements in x, y and z directions, respectively, at the location x of the beam reference axis; $\theta_x(x)$, $\theta_y(x)$ and $\theta_z(x)$ are the rotations about the x, y and z axes, respectively, at the location x of the beam reference axis; and $\psi_x(x)$, $\psi_y(x)$, and $\psi_z(x)$ are the shear rotations about the x, y and z axes, respectively, at the location x of the beam reference axis.

The corresponding infinitesimal strain field can be computed from Eq. (1) as:

$$\begin{cases} \varepsilon_{xx}(x,y,z) = \dfrac{du}{dx} = \underbrace{u_{o,x}(x)}_{\varepsilon_{xo}(x)} - y\underbrace{\theta_{z,x}(x)}_{\phi_z(x)} + z\underbrace{\theta_{y,x}(x)}_{\phi_y(x)} - y^3\psi_{z,x}(x) + z^3\psi_{y,x}(x) \\ \varepsilon_{yy}(x,y,z) = \dfrac{dv}{dy} = 0 \\ \varepsilon_{zz}(x,y,z) = \dfrac{dw}{dz} = 0 \\ \gamma_{xy}(x,y,z) = \dfrac{\partial u}{\partial y} + \dfrac{\partial v}{\partial x} = \underbrace{-\theta_z(x) + v_{o,x}(x)}_{\gamma_{xyo}(x)} - 3y^2\psi_z(x) - z\underbrace{\theta_{x,x}(x)}_{\phi_x(x)} + z\psi_{x,x}(x) \\ \gamma_{xz}(x,y,z) = \dfrac{\partial u}{\partial z} + \dfrac{\partial w}{\partial x} = \underbrace{\theta_y(x) + w_{o,x}(x)}_{\gamma_{xzo}(x)} + y\underbrace{\theta_{x,x}(x)}_{\phi_x(x)} + 3z^2\psi_y(x) + y\psi_{x,x}(x) \\ \gamma_{yz}(x,y,z) = \dfrac{\partial v}{\partial z} + \dfrac{\partial w}{\partial y} = 2\psi_x(x) \end{cases} \tag{2}$$

where the subscript "$,x$" represents the first derivative with respect to x; $\varepsilon_{xx}(x,y,z)$, $\varepsilon_{yy}(x,y,z)$ and $\varepsilon_{zz}(x,y,z)$ are the normal strains in the x, y and z directions, respectively; and $\gamma_{xy}(x,y,z)$, $\gamma_{xz}(x,y,z)$ and $\gamma_{yz}(x,y,z)$ are the independent engineering shear strains; $\varepsilon_{xo}(x)$ is the macroscopic axial section strain at the location x on the beam reference axis; $\phi_x(x)$, $\phi_y(x)$ and $\phi_z(x)$ are the macroscopic section curvatures about the x, y and z axes, respectively, at the location x on the beam reference axis; and $\gamma_{xyo}(x)$ and $\gamma_{xzo}(x)$ are the macroscopic shear section strains in y and z directions, respectively, at the location x on the beam reference axis (Fig. 1(a)).

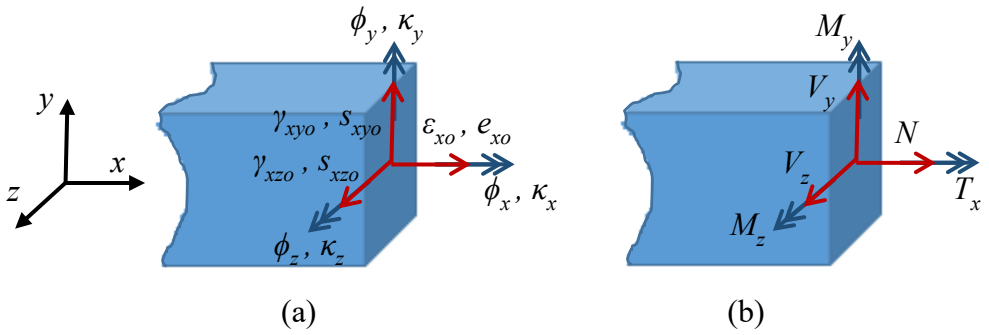

Fig. 1 – (a) Section strains; (b) section forces

Compared to the linear cross sectional displacement field obtained from Navier's assumption of plane sections, the 3rd order displacement field introduces three additional unknowns, namely, the shear rotations $\psi_x(x)$, $\psi_y(x)$ and $\psi_z(x)$. For a given cross-section shape and under the assumption of linearly elastic material response, these rotations can often be calculated by applying zero-traction conditions at the cross-section boundaries. This approach is often adopted in the analysis of framed structures because it eliminates the need to build beam element formulations with more than six degrees of freedom per node (Reddy 1997). For a rectangular solid cross-section, which is very common in RC structures, and for a beam reference axis passing through the cross-section centroid, there are zero tractions at the boundaries of the cross-section. These BCs would require:

$$\begin{cases} \sigma_{xy}(x, y=\pm h/2, z)=0 \\ \sigma_{yy}(x, y=\pm h/2, z)=0 \\ \sigma_{zy}(x, y=\pm h/2, z)=0 \end{cases} \text{ and } \begin{cases} \sigma_{xz}(x, y, z=\pm b/2)=0 \\ \sigma_{yz}(x, y, z=\pm b/2)=0 \\ \sigma_{zz}(x, y, z=\pm b/2)=0 \end{cases} \tag{3}$$

where b and h are the cross-section width and height, respectively. For a linear elastic beam, the shear stress BCs in Eq. (3) result in the following shear strain BCs:

$$\begin{cases} \gamma_{xy}(x, y=\pm h/2, z)=0 \\ \gamma_{xz}(x, y, z=\pm b/2)=0 \\ \gamma_{yz}(x, y, z=\pm b/2)=0 \end{cases} \tag{4}$$

Focusing on the special conditions $\gamma_{xy}(x, y=\pm h/2, z=0)=0$ and $\gamma_{xz}(x, y=0, z=\pm b/2)=0$, and according to Eq. (2), the shear rotations $\psi_x(x)$, $\psi_y(x)$ and $\psi_z(x)$ are obtained as:

$$\begin{cases} \psi_z(x) = \dfrac{4}{3h^2}\left(\gamma_{xyo}(x) - z\phi_x(x)\right) \\ \psi_y(x) = -\dfrac{4}{3b^2}\left(\gamma_{xzo}(x) + y\phi_x(x)\right) \\ \psi_x(x) = 0 \end{cases} \tag{5}$$

Because the strain field of Eq. (2) predicts zero lateral strains ($\varepsilon_{yy} = \varepsilon_{zz} = 0$), an unrealistically high confinement effect would always be predicted by this model. To capture the confinement effects more reasonably, the transverse strain components, ε_{yy} and ε_{zz}, are herein computed via through-the-depth cross-section equilibrium (Mullapudi and Ayoub 2012). The resulting equations, which express the equilibrium between the concrete and the transverse reinforcement, are enforced at any point located at the coordinates (x,y,z) as:

$$\begin{cases} \sigma_{cy}(x,y,z) + \rho_{sy}\sigma_{sy}(x,y,z) = 0 \\ \sigma_{cz}(x,y,z) + \rho_{sz}\sigma_{sz}(x,y,z) = 0 \\ \tau_{cyz}(x,y,z) = 0 \end{cases} \tag{6}$$

where σ_{cy} and σ_{cz} are the concrete stresses in y and z directions, respectively; σ_{sy} and σ_{sz} are the transverse steel stresses in y and z directions, respectively; τ_{cyz} is the yz-component of the concrete shear stresses; and ρ_{sy} and ρ_{sz} are the transverse steel ratios in y and z directions, respectively, which are assumed to be constant and independent of coordinates. In the above equations, σ_{cy} and σ_{cz} are computed from a multiaxial constitutive model (see next section), while σ_{sy} and σ_{sz} depend on ε_{yy} and ε_{zz}, respectively, through separate uniaxial constitutive models for the transverse steel. The latter models can be of any desired form (e.g., bilinear to capture the yielding of the transverse steel).

By substituting Eq. (5) into Eq. (2) and considering the above modification, the strain field becomes:

$$
\begin{cases}
\varepsilon_{xx}(x,y,z) = \varepsilon_{xo}(x) - y\phi_z(x) + z\phi_y(x) - \\
\qquad \dfrac{4y^3}{3h^2}\left(\gamma_{xyo,x}(x) - z\phi_{x,x}(x)\right) - \dfrac{4z^3}{3b^2}\left(\gamma_{xzo,x}(x) + y\phi_{x,x}(x)\right) \\
\varepsilon_{yy}(x,y,z): \text{Obtained from through-the-depth equilibrium} \\
\varepsilon_{zz}(x,y,z): \text{Obtained from through-the-depth equilibrium} \\
\gamma_{xy}(x,y,z) = \left(1 - \dfrac{4y^2}{h^2}\right)\left(\gamma_{xyo}(x) - z\phi_x(x)\right) \\
\gamma_{xz}(x,y,z) = \left(1 - \dfrac{4z^2}{b^2}\right)\left(\gamma_{xzo}(x) + y\phi_x(x)\right) \\
\gamma_{yz}(x,y,z) = \text{Obtained from through-the-depth equilibrium}
\end{cases}
\tag{7}
$$

This field is a function of the six macroscopic section strains/curvatures shown in Fig. 1(a), i.e., $\varepsilon_{xo}(x)$, $\phi_x(x)$, $\phi_y(x)$, $\phi_z(x)$, $\gamma_{xyo}(x)$ and $\gamma_{xzo}(x)$. It also includes the spatial derivatives of $\gamma_{xyo}(x)$ and $\gamma_{xzo}(x)$. While this field is valid for linear elastic beams, it is often used for the analysis of inelastic beams as well (Bhimaraddi and Chandrashekhara 1993; Ghugal and Sharma 2009).

4. Shear-Enhanced GI Element

4.1. Formulation

Similar to the original GI beam-column element formulation (Sideris and Salehi 2016; Salehi and Sideris 2017), the shear-enhanced formulation is based on four fundamental sets of equations, namely, macroscopic section strain-displacement equations, force equilibrium equations, section constitutive relations and nonlocality relations.

The *macroscopic section strain-displacement equations* relate the *macroscopic* section strains, ε_{xo}, ϕ_z, ϕ_y, γ_{xyo}, γ_{xzo} and ϕ_x, with the cross-section displacements/rotations along the beam reference axis, u_o, v_o, w_o, θ_x, θ_y and θ_z. According to Eq.(7), these equations are:

$$\begin{cases} \varepsilon_{xo}(x) = u_{o,x}(x) \\ \phi_z(x) = \theta_{z,x}(x) \\ \phi_y(x) = \theta_{y,x}(x) \\ \gamma_{xyo}(x) = v_{o,x}(x) - \theta_z(x) \\ \gamma_{xzo}(x) = w_{o,x}(x) + \theta_y(x) \\ \phi_x(x) = \theta_{x,x} \end{cases} \tag{8}$$

Neglecting inertial effects and body loads, the *force equilibrium equations* in the undeformed configuration of the beam are expressed in terms of the section forces as:

$$\begin{cases} N_{,x}(x) = 0 \\ V_{y,x}(x) = 0 \\ V_{z,x}(x) = 0 \\ M_{z,x}(x) + V_y(x) = 0 \\ M_{y,x}(x) - V_z(x) = 0 \\ T_{,x}(x) = 0 \end{cases} \tag{9}$$

where $N(x)$ is the axial force; $V_y(x)$ and $V_z(x)$ are the shear forces in y and z directions, respectively; $M_y(x)$ and $M_z(x)$ are the bending moments about the y and z axes; and $T(x)$ is the torsional moment; all at the location x along the beam reference axis (Fig. 1 (b)).

The *section constitutive relations* express the section forces, $\mathbf{D}(x)$, as a function of the *material* section strains, $\mathbf{d}^e(x)$, and their derivatives, $\mathbf{d}^e_{,x}(x)$, as:

$$\mathbf{D}(x) = \mathbf{f}_{ms}\left(\mathbf{d}^e(x), \mathbf{d}^e_{,x}(x)\right)$$

$$\text{with} \quad \begin{cases} \mathbf{D}(x) = \left[N(x) \quad M_z(x) \quad M_y(x) \quad V_y(x) \quad V_z(x) \quad T(x)\right]^T \\ \mathbf{d}^e(x) = \left[e_{xo}(x) \quad \kappa_z(x) \quad \kappa_y(x) \quad s_{xyo}(x) \quad s_{xzo}(x) \quad \kappa_x(x)\right]^T \\ \mathbf{d}^e_{,x}(x) = \left[e_{xo,x}(x) \quad \kappa_{z,x}(x) \quad \kappa_{y,x}(x) \quad s_{xyo,x}(x) \quad s_{xzo,x}(x) \quad \kappa_{x,x}(x)\right]^T \end{cases} \tag{10}$$

where $e_{xo}(x)$ is the *material* axial section strain; $\kappa_x(x)$, $\kappa_y(x)$ and $\kappa_z(x)$ are the *material* section curvatures about the x, y, and z axes, respectively; $s_{xyo}(x)$ and $s_{xzo}(x)$ are the *material* shear section strains in y and z directions, respectively (Fig. 1 (a)); and $\mathbf{f}_{ms}(.)$ is a vector function dependent on the cross-section material properties and dimensions. Unlike the original GI beam theory, for which $\mathbf{f}_{ms}(.)$ solely depends on $\mathbf{d}^e(x)$, in the shear-enhanced GI beam theory, $\mathbf{f}_{ms}(.)$ depends on both $\mathbf{d}^e(x)$ and $\mathbf{d}^e_{,x}(x)$ and the reasons are clarified below.

In order to build the relationship between $\mathbf{D}(x)$, $\mathbf{d}^e(x)$ and $\mathbf{d}^e_{,x}(x)$, i.e., the function $\mathbf{f}_{ms}(.)$, the material strain fields, $\mathbf{d}^e(x)$, are assumed to have the same forms as those of the macroscopic strains (see Eq. (7)), which yields:

$$\begin{cases} e_{xx}(x,y,z) = e_{xo}(x) - y\kappa_z(x) + z\kappa_y(x) - \dfrac{4y^3}{3h^2}s_{xyo,x}(x) - \dfrac{4z^3}{3b^2}s_{xzo,x}(x) \\ e_{yy}(x,y,z) = \varepsilon_{yy}(x,y,z) \\ e_{zz}(x,y,z) = \varepsilon_{zz}(x,y,z) \\ s_{xy}(x,y,z) = s_{xyo}(x)\left(1 - \dfrac{4y^2}{h^2}\right) - z\kappa_x(x) \\ s_{xz}(x,y,z) = s_{xzo}(x)\left(1 - \dfrac{4z^2}{b^2}\right) + y\kappa_x(x) \\ s_{yz}(x,y,z) = 0 \end{cases} \tag{11}$$

and furthermore the *macroscopic* and *material* normal transverse strains are assumed to be identical, i.e. $e_{yy}(x,y,z) = \varepsilon_{yy}(x,y,z)$ and $e_{zz}(x,y,z) = \varepsilon_{zz}(x,y,z)$ as shown above. The strains of Eq. (11) are used to calculate the stresses at any point over any cross-section of the beam via a 3D material model discussed later (Section 5.1). The section forces, $\mathbf{D}(x)$, can be calculated by integrating these stresses, which are acting on a cross-section, as:

$$\begin{cases} N(x) = \int \sigma_{xx}(x,y,z)\,dA \\ V_y(x) = \int \tau_{xy}(x,y,z)\,dA \\ V_z(x) = \int \tau_{xz}(x,y,z)\,dA \\ M_z(x) = \int -y\sigma_{xx}(x,y,z)\,dA \\ M_y(x) = \int z\sigma_{xx}(x,y,z)\,dA \\ T(x) = \int \left(y\tau_{xz}(x,y,z) - z\tau_{xy}(x,y,z)\right)dA \end{cases} \tag{12}$$

where $\sigma_{xx}(x,y,z)$ is the normal stress, $\tau_{xy}(x,y,z)$ is the shear stress in y direction, and $\tau_{xz}(x,y,z)$ is the shear stress in z direction, respectively, all of those acting at the coordinates (y, z) of the cross-section at the location x on the beam reference axis. These stresses are functions of the material strains over the cross-section, i.e., e_{xx}, e_{yy}, e_{zz}, s_{xy}, s_{xz} and s_{yz}, which are related to the material section strains, $\mathbf{d}^e(x)$, and its derivatives, $\mathbf{d}^e_{,x}(x)$, via Eqs. (11).

The *gradient nonlocality relations* associate the material section strains, $\mathbf{d}^e(x)$, with the macroscopic section strains, $\mathbf{d}(x)$, per Salehi and Sideris (2017), as:

$$\dot{\mathbf{d}}(x)-\frac{1}{2}l_c^2\dot{\mathbf{d}}_{,xx}H\left(W_s(x)\right)=\dot{\mathbf{d}}^e(x)$$
$$\text{with}\begin{cases}\mathbf{d}(x)=\left[\varepsilon_{xo}(x)\quad\phi_z(x)\quad\phi_y(x)\quad\gamma_{xyo}(x)\quad\gamma_{xzo}(x)\quad\phi_x(x)\right]^T\\ W_s(x)=\frac{1}{2}\dot{\mathbf{D}}(x)\cdot\dot{\mathbf{d}}^e(x)\end{cases}\tag{13}$$

where the overdot represents differentiation with respect to time, $\dot{\mathbf{d}}(x)$ and $\dot{\mathbf{d}}^e(x)$ are the rates of the macroscopic and material section strains, respectively; l_c is a characteristic length controlling the spread of damage/plasticity; $H(.)$ is the Heaviside step function; $\dot{\mathbf{D}}(x)$ is the rate of the section forces; and $W_s(x)$ is a quantity that is based on the material section strain energy density and is used to identify non-hardening section response. The two BCs to Eq. (13) are selected to be of the Dirichlet type and are applied at the beam ends Salehi and Sideris (2017). These BCs are expressed as:

$$\begin{cases}\dot{\mathbf{d}}(0)=\dot{\mathbf{d}}^e(0)\\ \dot{\mathbf{d}}(L)=\dot{\mathbf{d}}^e(L)\end{cases}\tag{14}$$

where L is the initial length of the element. Consistently, the spatial derivative of the material section strains, $\mathbf{d}^e_{,x}(x)$, which is also needed in the section constitutive relations (Eq. (10)), is taken to satisfy the nonlocality relations of Eq. (13) and thus obtained by the spatial derivatives of the macroscopic section strains, $\mathbf{d}_{,x}(x)$, as:

$$\dot{\mathbf{d}}_{,x}(x)-\frac{1}{2}l_c^2\dot{\mathbf{d}}_{,xxx}H\left(W_s(x)\right)=\dot{\mathbf{d}}^e_{,x}(x)\tag{15}$$

This approach ensures boundedness of the solution and response objectivity, i.e. convergence with mesh refinements. It is noted that direct differentiation of the *material* strain fields is not recommended, because they constitute an internal quantity whose smoothness cannot be guaranteed, thus often resulting in loss of the existence of spatial derivatives.

4.2. Analytical Solution

The GI FB beam-column element formulation is obtained from the exact analytical solution of the shear-enhanced GI beam theory. In this paper, a simply-supported reference beam with the force/displacement BCs shown in Fig. 2 is considered. With respect to the selected six force

BCs, the force equilibrium equations (Eq. (9)) can be solved analytically for the section forces, $\mathbf{D}(x)$, as:

$$\mathbf{D}(x)=\mathbf{b}(x)\mathbf{Q} \quad \text{with} \quad \begin{cases} \mathbf{Q}=\begin{bmatrix} Q_1 & Q_2 & Q_3 & Q_4 & Q_5 & Q_6 \end{bmatrix} \\ \mathbf{b}(x)=\begin{bmatrix} 1 & 0 & 0 & 0 & 0 & 0 \\ 0 & x/L & x/L-1 & 0 & 0 & 0 \\ 0 & 0 & 0 & x/L & x/L-1 & 0 \\ 0 & -1/L & -1/L & 0 & 0 & 0 \\ 0 & 0 & 0 & 1/L & 1/L & 0 \\ 0 & 0 & 0 & 0 & 0 & 1 \end{bmatrix} \end{cases} \tag{16}$$

where $\mathbf{Q}$ is the vector of the force BCs; and $\mathbf{b}(x)$ is the matrix of the force shape functions.

The corresponding end displacement BCs, $\mathbf{q}$, (see Fig. 2), are obtained from the macroscopic section strains, $\mathbf{d}(x)$, through direct integration of Eqs. (8) as:

$$\mathbf{q}=\int_0^L \mathbf{b}(x)^T\,\mathbf{d}(x)\,dx \quad \text{with} \quad \mathbf{q}=\begin{bmatrix} q_1 & q_2 & q_3 & q_4 & q_5 & q_6 \end{bmatrix}^T \tag{17}$$

The solution of the gradient nonlocality relations of Eq. (13) with the BCs of Eq. (14) may be assumed to have the following generic form:

$$\dot{\mathbf{d}}(x)=\mathbf{f}_{nl}\left(\dot{\mathbf{d}}^e(x)\right) \tag{18}$$

where $\mathbf{f}_{nl}(.)$ is a general solution. By substituting Eq. (16) into Eq. (10), the system of equations representing the analytical form of the shear-enhanced GI FB element formulation is obtained:

$$\begin{cases} \mathbf{b}(x)\mathbf{Q}-\mathbf{f}_{ms}\left(\mathbf{d}^e(x),\mathbf{d}^e_{,x}(x)\right)=\mathbf{0} \\ \mathbf{q}-\int_0^L \mathbf{b}(x)^T\,\mathbf{d}(x)\,dx=\mathbf{0} \end{cases} \tag{19}$$

The material section strains, $\mathbf{d}^e(x)$, and the end forces, $\mathbf{Q}$, are the two unknowns of the above system of two equations for given end displacements, $\mathbf{q}$. The macroscopic section strain rates, $\dot{\mathbf{d}}(x)$, can be explicitly computed from Eq. (18), while the total macroscopic section strains are calculated from the time integration of $\dot{\mathbf{d}}(x)$. Similarly, the spatial derivative of the *material* section strains, $\mathbf{d}^e_{,x}(x)$, is computed through Eq. (15)..

Fig. 2 – Simply-supported reference beam and its associated displacement/force boundary conditions

4.3. Discretization and Numerical Solution

Due to the nonlinearity of the section constitutive relations of Eq. (10) and the impracticality of the explicit analytical solution of the gradient nonlocality relations of Eq. (13), Eqs. (19) have to be evaluated at spatially discrete locations, x_i, and numerically solved at discrete time instants, t_k (k denotes the time step). In the discretization process, the force equilibrium equations (first of Eq. (19)) should be satisfied at the discrete locations, while the integral of the displacement compatibility equations (second of Eq. (19)) is approximated through a numerical integration scheme. With N IPs (i = 1, 2, …, N), the discretized form of Eq. (19) at the time instant t_k is:

$$\begin{cases} \begin{cases} \mathbf{b}\left(x_1\right)\mathbf{Q}_k - \mathbf{f}_{ms}\left(\mathbf{d}_k^e\left(x_1\right), \mathbf{d}_{k,x}^e\left(x_1\right)\right) = \mathbf{0} \\ \mathbf{b}\left(x_2\right)\mathbf{Q}_k - \mathbf{f}_{ms}\left(\mathbf{d}_k^e\left(x_2\right), \mathbf{d}_{k,x}^e\left(x_2\right)\right) = \mathbf{0} \\ \quad\vdots \qquad\qquad \vdots \qquad\qquad \vdots \\ \mathbf{b}\left(x_N\right)\mathbf{Q}_k - \mathbf{f}_{ms}\left(\mathbf{d}_k^e\left(x_N\right), \mathbf{d}_{k,x}^e\left(x_N\right)\right) = \mathbf{0} \end{cases} \\ \mathbf{q}_k - \sum_{i=1}^{N} w_i \mathbf{b}\left(x_i\right)^T \mathbf{d}_k\left(x_i\right) = \mathbf{0} \end{cases} \tag{20}$$

where $x_1 = 0$ and $x_N = L$, and w_i is the integration weight at x_i with $\sum_{i=1}^{N} w_i = L$.

By enforcing the nonlocality relations of Eq. (13) at discrete locations and replacing the second spatial derivative with its 2nd-order accurate finite difference approximation, the following relation is obtained in a discretized form between the macroscopic and material section strain rates at the location x_i (ith IP) and at the time t_k:

$$\dot{\mathbf{d}}_k\left(x_i\right) - \frac{1}{2} l_c^2 \left[\frac{\dot{\mathbf{d}}_k\left(x_{i+1}\right) - 2\dot{\mathbf{d}}_k\left(x_i\right) + \dot{\mathbf{d}}_k\left(x_{i-1}\right)}{\left(\Delta x\right)^2} \right] H\left(W_{s,k}\left(x_i\right)\right) = \dot{\mathbf{d}}_k^e\left(x_i\right) \tag{21}$$

where Δx is the spacing between adjacent IPs, which are assumed to be equally spaced. In addition, applying the Dirichlet BCs of Eq. (14) gives:

$$\begin{cases} \dot{\mathbf{d}}_k\left(x_1\right) = \dot{\mathbf{d}}_k^e\left(x_1\right) \\ \dot{\mathbf{d}}_k\left(x_N\right) = \dot{\mathbf{d}}_k^e\left(x_N\right) \end{cases} \tag{22}$$

If $W_{s,k}(x_i) > 0$ for all discrete locations (i.e., no localization is identified over the element), combining the first of Eq. (21) with Eq. (22) yields:

$$\begin{aligned} &\dot{\mathbf{d}}_{tot,k} = \mathbf{H}_k^{-1}\dot{\mathbf{d}}_{tot,k}^e\left(x_i\right) \\ &\text{with } \begin{cases} \dot{\mathbf{d}}_{tot,k}^e = \left[\dot{\mathbf{d}}_k^{eT}\left(x_1\right) \quad \dot{\mathbf{d}}_k^{eT}\left(x_2\right) \quad \cdots \quad \dot{\mathbf{d}}_k^{eT}\left(x_N\right)\right]^T \\ \dot{\mathbf{d}}_{tot,k} = \left[\dot{\mathbf{d}}_k^{T}\left(x_1\right) \quad \dot{\mathbf{d}}_k^{T}\left(x_2\right) \quad \cdots \quad \dot{\mathbf{d}}_k^{T}\left(x_N\right)\right]^T \end{cases} \end{aligned} \tag{23}$$

where the material and macroscopic section strain rates at all IPs are included in the vectors $\dot{\mathbf{d}}_{tot,k}^e$ and $\dot{\mathbf{d}}_{tot,k}$, respectively, and $\mathbf{H}_k$ is a $6N \times 6N$ matrix defined as:

$$\mathbf{H}_k = \begin{bmatrix} \mathbf{I}_{6\times6} & \mathbf{O}_{6\times6} & & & \\ B_c\mathbf{I}_{6\times6} & A_c\mathbf{I}_{6\times6} & B_c\mathbf{I}_{6\times6} & & \\ & \ddots & \ddots & \ddots & \\ & & B_c\mathbf{I}_{6\times6} & A_c\mathbf{I}_{6\times6} & B_c\mathbf{I}_{6\times6} \\ & & & \mathbf{O}_{6\times6} & \mathbf{I}_{6\times6} \end{bmatrix} \quad \text{with} \quad \begin{cases} A_c = 1 + \left(\dfrac{l_c}{\Delta x}\right)^2 \\ B_c = -\dfrac{1}{2}\left(\dfrac{l_c}{\Delta x}\right)^2 \end{cases} \tag{24}$$

where $\mathbf{I}_{6\times6}$ and $\mathbf{O}_{6\times6}$ are 6×6 identity and zero matrices, respectively, A_c and B_c are constants, and the discretized form of $W_{s,k}(x_i)$ is:

$$W_{s,k}\left(x_i\right) = \frac{1}{2}\left[\mathbf{D}_k\left(x_i\right) - \mathbf{D}_{k-1}\left(x_i\right)\right] \cdot \left[\mathbf{d}_k^e\left(x_i\right) - \mathbf{d}_{k-1}^e\left(x_i\right)\right] \tag{25}$$

Upon localization identification at an IP of coordinate x_i, at the time instant t_k, i.e., when $W_{s,k}(x_i) \leq 0$ in Eq. (21), the corresponding rows of $\mathbf{H}_k$ are replaced with zeros, except for the diagonal elements, which are replaced with unities. Using explicit time discretization, the total macroscopic section strains at t_k are obtained as $\mathbf{d}_{tot,k} = \mathbf{d}_{tot,k-1} + \mathbf{H}_{k-1}^{-1}\left(\mathbf{d}_{tot,k}^e - \mathbf{d}_{tot,k-1}^e\right)$. The explicit discretization is used because calculation of $\mathbf{H}$ requires knowledge of the section forces, which are function of the spatial derivatives of the macroscopic strains. This would require an internal set of iterations, which is herein bypassed by this explicit discretization.

Similarly, Eq. (15) can also be discretized using 2nd-order accurate finite difference approximations, which have different forms depending on the IP location, as:

$$\begin{cases}
\left(\frac{-3\dot{\mathbf{d}}_k(x_i)+4\dot{\mathbf{d}}_k(x_{i+1})-\dot{\mathbf{d}}_k(x_{i+2})}{2\Delta x}\right)-\frac{1}{2}l_c^2\left(\frac{-5\dot{\mathbf{d}}_k(x_i)+18\dot{\mathbf{d}}_k(x_{i+1})-24\dot{\mathbf{d}}_k(x_{i+2})+14\dot{\mathbf{d}}_k(x_{i+3})-3\dot{\mathbf{d}}_k(x_{i+4})}{2(\Delta x)^3}\right)=\dot{\mathbf{d}}^e_{k,x}(x_i), & i=1\\
\left(\frac{-\dot{\mathbf{d}}_k(x_{i-1})+\dot{\mathbf{d}}_k(x_{i+1})}{2\Delta x}\right)-\frac{1}{2}l_c^2\left(\frac{-3\dot{\mathbf{d}}_k(x_{i-1})+10\dot{\mathbf{d}}_k(x_i)-12\dot{\mathbf{d}}_k(x_{i+1})+6\dot{\mathbf{d}}_k(x_{i+2})-\dot{\mathbf{d}}_k(x_{i+3})}{2(\Delta x)^3}\right)=\dot{\mathbf{d}}^e_{k,x}(x_i), & i=2\\
\left(\frac{-\dot{\mathbf{d}}_k(x_{i-1})+\dot{\mathbf{d}}_k(x_{i+1})}{2\Delta x}\right)-\frac{1}{2}l_c^2\left(\frac{-\dot{\mathbf{d}}_k(x_{i-2})+2\dot{\mathbf{d}}_k(x_{i-1})-2\dot{\mathbf{d}}_k(x_{i+1})+\dot{\mathbf{d}}_k(x_{i+2})}{2(\Delta x)^3}\right)=\dot{\mathbf{d}}^e_{k,x}(x_i), & 3\le i\le N-2\\
\left(\frac{-\dot{\mathbf{d}}_k(x_{i-1})+\dot{\mathbf{d}}_k(x_{i+1})}{2\Delta x}\right)-\frac{1}{2}l_c^2\left(\frac{\dot{\mathbf{d}}_k(x_{i-3})-6\dot{\mathbf{d}}_k(x_{i-2})+12\dot{\mathbf{d}}_k(x_{i-1})-10\dot{\mathbf{d}}_k(x_i)+3\dot{\mathbf{d}}_k(x_{i+1})}{2(\Delta x)^3}\right)=\dot{\mathbf{d}}^e_{k,x}(x_i), & i=N-1\\
\left(\frac{\dot{\mathbf{d}}_k(x_{i-2})-4\dot{\mathbf{d}}_k(x_{i-1})+3\dot{\mathbf{d}}_k(x_i)}{2\Delta x}\right)-\frac{1}{2}l_c^2\left(\frac{3\dot{\mathbf{d}}_k(x_{i-4})-14\dot{\mathbf{d}}_k(x_{i-3})+24\dot{\mathbf{d}}_k(x_{i-2})-18\dot{\mathbf{d}}_k(x_{i-1})+5\dot{\mathbf{d}}_k(x_i)}{2(\Delta x)^3}\right)=\dot{\mathbf{d}}^e_{k,x}(x_i), & i=N
\end{cases} \quad (26)$$

Through these discretizations, a matrix form is built as: $\mathbf{G}\,\dot{\mathbf{d}}_{tot,k,x}=\dot{\mathbf{d}}^e_{tot,k,x}$, where $\mathbf{G}$ is the differential finite difference operator matrix, which is constant. The spatial derivative of material section strains, which are used in the section constitutive relations (Eq. (10)), can then be numerically computed as $\mathbf{d}^e_{tot,k,x}=\mathbf{d}^e_{tot,k-1,x}+\mathbf{G}\left(\mathbf{d}_{tot,k,x}-\mathbf{d}_{tot,k-1,x}\right)$. The above discretization scheme also implies that a shear-enhanced GI element should include at least five integration points.

The condensed discretized form of Eq. (20) at t_k can be written as:

$$\begin{cases}\mathbf{B}_Q\mathbf{Q}_k-\mathbf{F}_{ms}\left(\mathbf{d}^e_{tot,k},\mathbf{d}^e_{tot,k,x}\right)=\mathbf{0}\\ \mathbf{q}_k-\mathbf{B}_q\mathbf{d}_{tot,k}=\mathbf{0}\end{cases} \quad (27)$$

with

$$\mathbf{B}_Q=\begin{bmatrix}\mathbf{b}(x_1)\\ \mathbf{b}(x_2)\\ \vdots\\ \mathbf{b}(x_N)\end{bmatrix}_{6N\times 6},\ \mathbf{F}_{ms}\left(\mathbf{d}^e_{tot,k}\right)=\begin{Bmatrix}\mathbf{f}_{ms}\left(\mathbf{d}^e_k(x_1),\mathbf{d}^e_{k,x}(x_1)\right)\\ \mathbf{f}_{ms}\left(\mathbf{d}^e_k(x_2),\mathbf{d}^e_{k,x}(x_2)\right)\\ \vdots\\ \mathbf{f}_{ms}\left(\mathbf{d}^e_k(x_N),\mathbf{d}^e_{k,x}(x_N)\right)\end{Bmatrix}_{6N\times 1} \quad (28)$$

$$\mathbf{B}_q=\begin{bmatrix}w_1\mathbf{b}(x_1)^T & w_2\mathbf{b}(x_2)^T & \cdots & w_N\mathbf{b}(x_N)^T\end{bmatrix}_{6\times 6N}$$

where $\mathbf{F}_{ms}(.)$ is the vector of internal section forces, which are function of the material section strains, $\mathbf{d}^e_{tot,k}$ and their derivatives, $\mathbf{d}^e_{tot,k,x}$; $\mathbf{B}_Q$ is the time-invariant matrix of discretized force shape functions; and $\mathbf{B}_q$ is the time-invariant matrix of macroscopic section strain integration.

The material section strains, $\mathbf{d}^e_{tot,k}$, and the force BCs, $\mathbf{Q}_k$, can be computed for given displacement BCs, $\mathbf{q}_k$, through a Newton-Raphson iterative scheme as follows:

$$\begin{Bmatrix} \mathbf{Q}_k \\ \mathbf{d}^e_{tot,k} \end{Bmatrix}_{j+1} = \begin{Bmatrix} \mathbf{Q}_k \\ \mathbf{d}^e_{tot,k} \end{Bmatrix}_j - \begin{bmatrix} \mathbf{B}_Q & -\mathbf{K}_{ms,k} \\ \mathbf{O}_{6\times 6} & -\mathbf{B}_q \mathbf{H}_k^{-1} \end{bmatrix}_j^{-1} \begin{Bmatrix} \mathbf{B}_Q \mathbf{Q}_k - \mathbf{F}_{ms}\left(\mathbf{d}^e_{tot,k}, \mathbf{d}^e_{tot,k,x}\right) \\ \mathbf{q}_k - \mathbf{B}_q \mathbf{d}_{tot,k} \end{Bmatrix}_j \tag{29}$$

where $\mathbf{K}_{ms,k}$ is the matrix of total tangential section stiffness at the time t_k, defined as:

$$\mathbf{K}_{ms,k} = \begin{bmatrix} \mathbf{k}_{ms,k}(x_1) & \mathbf{O}_{6\times 6} & \cdots & \mathbf{O}_{6\times 6} \\ \mathbf{O}_{6\times 6} & \mathbf{k}_{ms,k}(x_2) & \cdots & \mathbf{O}_{6\times 6} \\ \vdots & \vdots & \ddots & \vdots \\ \mathbf{O}_{6\times 6} & \mathbf{O}_{6\times 6} & \cdots & \mathbf{k}_{ms,k}(x_N) \end{bmatrix} \tag{30}$$

with $\mathbf{k}_{ms,k}(x_i)$ representing the tangent stiffness matrix at the location x_i (ith IP) at the time t_k. It is noted that in order to maintain simplicity, the Jacobian in Eq. (29) is approximate, because it does not include the effect of $\mathbf{d}^e_{tot,k,x}$. This approach was found to provide acceptable convergence rates.

5. Concrete Constitutive Model

5.1. Formulation

Due to the interactions between concrete and steel bars in RC elements, the response of plain concrete is different than the concrete's response in the presence of steel reinforcement. Major response differences that are manifested in RC members include two phenomena, namely, tension stiffening and compression softening. Tension stiffening refers to the contribution of the steel reinforcement in the apparent stress transfer by concrete tension cracks which results in a much slower degradation (as opposed to brittle degradation) of the concrete stress-strain response in the post-peak tensile range (Floegl and Mang 1982; Massicotte et al. 1990). Compression softening refers to the reduction in the compressive strength of concrete in one direction due to large tensile stresses in the orthogonal direction (Vecchio and Collins 1986; Hsu 1988). Reasonable representation of both of these phenomena is important in modeling axial-flexural-shear interactions of RC elements. Tension stiffening is often simulated by adjusting the material parameters that control the post-peak tensile response of concrete material laws. However, in this study, this phenomenon is more naturally reproduced by the through-the-depth equilibrium, which explicitly accounts for the effect of the transverse reinforcement on the concrete response, while the longitudinal reinforcement is also accounted for through the axial and flexural beam equilibrium. Compression softening will be herein accounted for via an additional damage factor.

The proposed 3D constitutive model is developed to predict the concrete stress components at any point on the cross section, $\boldsymbol{\sigma} = \begin{bmatrix} \sigma_{xx} & \sigma_{yy} & \sigma_{zz} & \tau_{xy} & \tau_{xz} & \tau_{yz} \end{bmatrix}^T$, as a function of corresponding material strain components, $\mathbf{e} = \begin{bmatrix} e_{xx} & e_{yy} & e_{zz} & s_{xy} & s_{xz} & s_{yz} \end{bmatrix}^T$, where s_{xy}, s_{xz} and s_{yz} are *engineering* shear strains. The proposed constitutive laws adopt the widely used concrete damage plasticity model proposed by Lee and Fenves (1998) and modify it by including compression softening effects and by removing the fracture energy-based re-scaling conditions with the element size, because objectivity is treated at the element-level via the gradient inelastic beam mechanics.

In the proposed model, the total material strains, **e**, are additively decomposed into an elastic and a plastic material strain component as: $\mathbf{e} = \mathbf{e}_{el} + \mathbf{e}_{pl}$, with $\mathbf{e}_{el}$ and $\mathbf{e}_{pl}$ being the vector of the elastic and plastic material strains, respectively. Stiffness/modulus degradation is coupled with classical plasticity, resulting in the stress vector as:

$$\boldsymbol{\sigma} = (1-D)\,\overline{\boldsymbol{\sigma}} = (1-D)\,\mathbf{E}\mathbf{e}_{el} \tag{31}$$

where D is a scalar isotropic degradation damage factor with $0 \le D \le 1$, $\overline{\boldsymbol{\sigma}}$ is the effective stress vector of the undamaged material, and **E** is the elastic (undamaged) modulus matrix which is given as:

$$\mathbf{E} = \frac{E}{(1+\nu)(1-2\nu)} \begin{bmatrix} 1-\nu & \nu & \nu & 0 & 0 & 0 \\ \nu & 1-\nu & \nu & 0 & 0 & 0 \\ \nu & \nu & 1-\nu & 0 & 0 & 0 \\ 0 & 0 & 0 & \dfrac{1-2\nu}{2} & 0 & 0 \\ 0 & 0 & 0 & 0 & \dfrac{1-2\nu}{2} & 0 \\ 0 & 0 & 0 & 0 & 0 & \dfrac{1-2\nu}{2} \end{bmatrix} \tag{32}$$

where E is the Young's modulus and ν is the Poisson's ratio.

The damage factor, D, is determined as:

$$D = 1-(1-D_t)\left((1-D_c)\,\beta_{ct}\right) \tag{33}$$

where D_t and D_c are the tension and compression damage factors ($0 \le D_t, D_c \le 1$), which are determined as:

$$\begin{cases} D_t = 1 - \exp\left(-d_t \kappa_t\right) \\ D_c = 1 - \exp\left(-d_c \kappa_c\right) \end{cases} \tag{34}$$

where κ_t and κ_c are damage variables that represent accumulated straining in tension and compression, respectively, and are discussed later, while d_t and d_c are nonnegative damage constants that control the rate of degradation for tension and compression damage. Also, β_{ct} is a compression softening factor ($0 < \beta_{ct} \leq 1$), which is based on Hsu (1988) as simplified by Feng et al. (2018). In the present paper, the principal tensile strain used to compute β_{ct} in the above studies (Hsu 1988; Feng et al. 2018) is replaced with the accumulated straining in tension, κ_t, as shown below:

$$\beta_{ct} = \frac{1.0}{\sqrt{1 + d_{ct} \kappa_t}} \tag{35}$$

which makes β_{ct} representative of the accumulated influence of compression softening under reversed loading taking place under complex multiaxial stress/strain conditions.

The adopted ***yield criterion*** is given by Lubliner et al. (1989) as:

$$F\left(\bar{\boldsymbol{\sigma}}, \boldsymbol{\kappa}\right) = \frac{1}{1-\alpha}\left(\alpha \bar{I}_1 + \sqrt{3\bar{J}_2} + \beta\left(\boldsymbol{\kappa}\right)\left\langle \hat{\bar{\sigma}}_{\max} \right\rangle - \gamma \left\langle -\hat{\bar{\sigma}}_{\max} \right\rangle\right) - \bar{C}_c\left(\kappa_c\right) \tag{36}$$

with:

$$\begin{cases} \gamma = 3\dfrac{1-K_c}{2K_c - 1} \\ \beta\left(\boldsymbol{\kappa}\right) = \dfrac{\bar{C}_c\left(\kappa_c\right)}{\bar{C}_t\left(\kappa_t\right)}\left(1-\alpha\right) - \left(1+\alpha\right) \\ \alpha = \dfrac{f_{bo} - f_{co}}{2f_{bo} - f_{co}} \end{cases} \tag{37}$$

where $\boldsymbol{\kappa} = \begin{bmatrix} \kappa_t & \kappa_c \end{bmatrix}^T$, $\bar{I}_1$ is the first invariant of the effective stress tensor; $\bar{J}_2$ is the second invariant of the deviatoric effective stress tensor; α, $\beta\left(\boldsymbol{\kappa}\right)$ and γ are dimensionless constants with $0 \leq \alpha \leq 0.5$; K_c is the ratio of the second stress invariant on the tensile meridian to that on the compressive meridian with $0.5 < K_c < 1.0$; $\hat{\bar{\sigma}}_{\max}$ is the peak algebraic principal effective stress (positive in tension); f_{bo} is biaxial initial yield compressive stress; f_{co} is the uniaxial initial yield compressive stress; and $\bar{C}_c\left(\kappa_c\right)$ and $\bar{C}_t\left(\kappa_t\right)$ are effective compressive and tensile cohesion strengths, respectively, which are functions of the damage variables κ_c and κ_t,

respectively. Per Lubliner et al. (1989), the cohesion strengths in the total stress domain may be expressed as:

$$\begin{cases} C_t\left(\kappa_t\right) = f_{t0}\left[\left(1+a_t\right)\exp(-b_t\kappa_t) - a_t\exp\left(-2b_t\kappa_t\right)\right] \\ C_c\left(\kappa_c\right) = f_{c0}\left[\left(1+a_c\right)\exp(-b_c\kappa_c) - a_c\exp\left(-2b_c\kappa_c\right)\right] \end{cases} \tag{38}$$

Based on Eq. (31), the cohesion strengths can be expressed in the effective stress space as:

$$\begin{cases} \overline{C}_c\left(\kappa_c\right) = C_c\left(\kappa_c\right)/\left(1-D_c\right) \\ \overline{C}_t\left(\kappa_t\right) = C_t\left(\kappa_t\right)/\left(1-D_t\right) \end{cases} \tag{39}$$

The adopted ***flow rule*** is expressed as:

$$\dot{\mathbf{e}}_{pl}^{e} = \dot{\lambda}\,\mathbf{m}\left(\overline{\boldsymbol{\sigma}}\right) = \dot{\lambda}\frac{\partial\Phi\left(\overline{\boldsymbol{\sigma}}\right)}{\partial\overline{\boldsymbol{\sigma}}} \tag{40}$$

where λ is the plastic multiplier and $\Phi\left(\overline{\boldsymbol{\sigma}}\right)$ is the hyperbolic form of the Drucker-Prager plastic potential computed as:

$$\Phi\left(\overline{\boldsymbol{\sigma}}\right) = \sqrt{\left(3\alpha_p\rho f_{t0}\right)^2 + 3\overline{J}_2} + \alpha_p\overline{I}_1 \tag{41}$$

with f_{t0} is the uniaxial tensile yield stress, ρ is the eccentricity parameter and a_p (= tanψ) is a constant that represents the dilatancy of concrete with ψ being the dilation angle.

The evolution of the damage variables κ_t and κ_c, is determined in rate form as:

$$\dot{\boldsymbol{\kappa}} = \dot{\lambda}\mathbf{H}\left(\hat{\overline{\boldsymbol{\sigma}}}\right) \tag{42}$$

where $\mathbf{H}\left(\hat{\overline{\boldsymbol{\sigma}}}\right)$ is a plastic modulus given as:

$$\mathbf{H}\left(\hat{\overline{\boldsymbol{\sigma}}}\right) = \begin{bmatrix} r\left(\hat{\overline{\boldsymbol{\sigma}}}\right) & 0 & 0 \\ 0 & 0 & -\left(1-r\left(\hat{\overline{\boldsymbol{\sigma}}}\right)\right) \end{bmatrix}\frac{\partial\Phi\left(\overline{\boldsymbol{\sigma}}\right)}{\partial\hat{\overline{\boldsymbol{\sigma}}}} \tag{43}$$

with the weight function $r\left(\hat{\overline{\boldsymbol{\sigma}}}\right)$ being defined as:

$$r\left(\hat{\overline{\boldsymbol{\sigma}}}\right) = \begin{cases} 0 & \text{if } \hat{\overline{\boldsymbol{\sigma}}} = \mathbf{0} \\ \dfrac{\left(\sum_{i=1}^{3}\left\langle\hat{\overline{\sigma}}_i\right\rangle\right)}{\left(\sum_{i=1}^{3}\left|\hat{\overline{\sigma}}_i\right|\right)} & \text{otherwise} \end{cases} \tag{44}$$

In Eq. (42) through (44), $\hat{\bar{\boldsymbol{\sigma}}}$ is the vector of the principal effective stresses, i.e., $\hat{\bar{\boldsymbol{\sigma}}} = \begin{bmatrix} \hat{\bar{\sigma}}_1 & \hat{\bar{\sigma}}_2 & \hat{\bar{\sigma}}_3 \end{bmatrix}^T$ with $\hat{\bar{\sigma}}_1 \geq \hat{\bar{\sigma}}_2 \geq \hat{\bar{\sigma}}_3$.

5.2. Calculation of Tangent

The tangent of stress vs. strain model is computed through direct differentiation as:

$$\frac{\partial \boldsymbol{\sigma}}{\partial \mathbf{e}} = (1-D)\frac{\partial \bar{\boldsymbol{\sigma}}}{\partial \mathbf{e}} - \bar{\boldsymbol{\sigma}}\frac{\partial D}{\partial \mathbf{e}} \tag{45}$$

For elastic response $(\dot{\lambda} = 0)$:

$$\frac{\partial D}{\partial \mathbf{e}} = \mathbf{0} \Rightarrow \frac{\partial \boldsymbol{\sigma}}{\partial \mathbf{e}} = (1-D)\mathbf{E} \tag{46}$$

For inelastic response $(\dot{\lambda} > 0)$, the consistency condition, $\dot{\lambda}\dot{F}_{ys} = 0$, is adopted to find the relation between $\dot{\lambda}$, $\dot{\bar{\boldsymbol{\sigma}}}$, and $\dot{\boldsymbol{\varepsilon}}$, as:

$$\dot{F}_{ys}(\bar{\boldsymbol{\sigma}}, \boldsymbol{\kappa}) = \frac{\partial F_{ys}}{\partial \bar{\boldsymbol{\sigma}}}\dot{\bar{\boldsymbol{\sigma}}} + \frac{\partial F_{ys}}{\partial \boldsymbol{\kappa}}\frac{\partial \boldsymbol{\kappa}}{\partial \lambda}\dot{\lambda} = 0 \tag{47}$$

and solving for $\dot{\lambda}$:

$$\dot{\lambda} = -\left(\frac{\partial F_{ys}}{\partial \boldsymbol{\kappa}}\frac{\partial \boldsymbol{\kappa}}{\partial \lambda}\right)^{-1}\left(\frac{\partial F_{ys}}{\partial \bar{\boldsymbol{\sigma}}}\right)\dot{\bar{\boldsymbol{\sigma}}} \tag{48}$$

which, using $\dot{\boldsymbol{\sigma}} = \mathbf{E}(\dot{\mathbf{e}} - \dot{\mathbf{e}}^p)$, further becomes:

$$\dot{\lambda} = -\left(\frac{\partial F_{ys}}{\partial \boldsymbol{\kappa}}\frac{\partial \boldsymbol{\kappa}}{\partial \lambda}\right)^{-1}\left(\frac{\partial F_{ys}}{\partial \bar{\boldsymbol{\sigma}}}\right)\mathbf{E}\left(\dot{\mathbf{e}} - \underbrace{\dot{\mathbf{e}}^p}_{\dot{\lambda}\frac{\partial \Phi(\bar{\boldsymbol{\sigma}})}{\partial \bar{\boldsymbol{\sigma}}}}\right) \tag{49}$$

and further using Eq. (**40**) gives:

$$\dot{\lambda} = \left(\frac{\partial F_{ys}}{\partial \bar{\boldsymbol{\sigma}}}\mathbf{E}\frac{\partial \Phi(\bar{\boldsymbol{\sigma}})}{\partial \bar{\boldsymbol{\sigma}}} - \frac{\partial F_{ys}}{\partial \boldsymbol{\kappa}}\frac{\partial \boldsymbol{\kappa}}{\partial \lambda}\right)^{-1}\left(\frac{\partial F_{ys}}{\partial \bar{\boldsymbol{\sigma}}}\mathbf{E}\right)\dot{\mathbf{e}} \tag{50}$$

By substituting Eq. (50) into Eq. (47), we get:

$$\frac{\partial \bar{\boldsymbol{\sigma}}}{\partial \mathbf{e}} = \left(\mathbf{E}^{-1} - \frac{\partial \Phi(\bar{\boldsymbol{\sigma}})}{\partial \bar{\boldsymbol{\sigma}}}\left(\frac{\partial F_{ys}}{\partial \boldsymbol{\kappa}}\frac{\partial \boldsymbol{\kappa}}{\partial \lambda}\right)^{-1}\left(\frac{\partial F_{ys}}{\partial \bar{\boldsymbol{\sigma}}}\right)\right)^{-1}_{6\times 6} \tag{51}$$

The rate of the damage factor can be calculated as:

$$\dot{D} = \frac{\partial D}{\partial \boldsymbol{\kappa}} \frac{\partial \boldsymbol{\kappa}}{\partial \lambda} \dot{\lambda} \tag{52}$$

and using Eq. (50):

$$\dot{D} = \frac{\partial D}{\partial \boldsymbol{\kappa}} \frac{\partial \boldsymbol{\kappa}}{\partial \lambda} \left(\frac{\partial F_{ys}}{\partial \overline{\boldsymbol{\sigma}}} \mathbf{E} \frac{\partial \Phi(\overline{\boldsymbol{\sigma}})}{\partial \overline{\boldsymbol{\sigma}}} - \frac{\partial F_{ys}}{\partial \boldsymbol{\kappa}} \frac{\partial \boldsymbol{\kappa}}{\partial \lambda} \right)^{-1} \left(\frac{\partial F_{ys}}{\partial \overline{\boldsymbol{\sigma}}} \mathbf{E} \right) \dot{\mathbf{e}} \tag{53}$$

resulting in:

$$\frac{\partial D}{\partial \mathbf{e}} = \left(\frac{\partial D}{\partial \boldsymbol{\kappa}} \frac{\partial \boldsymbol{\kappa}}{\partial \lambda} \right) \left(\frac{\partial F_{ys}}{\partial \overline{\boldsymbol{\sigma}}} \mathbf{E} \frac{\partial \Phi(\overline{\boldsymbol{\sigma}})}{\partial \overline{\boldsymbol{\sigma}}} - \frac{\partial F_{ys}}{\partial \boldsymbol{\kappa}} \frac{\partial \boldsymbol{\kappa}}{\partial \lambda} \right)^{-1} \left(\frac{\partial F_{ys}}{\partial \overline{\boldsymbol{\sigma}}} \mathbf{E} \right) \tag{54}$$

By substituting Eqs. (51) and (54) into Eq. (45), the tangent of the stress vs. strain model is obtained.

5.3. Numerical Solution of Concrete Constitutive Relations

At each cross-sectional fiber that is represented by a concrete constitutive model, the variables $\left\{ \boldsymbol{\sigma}_k, \mathbf{e}_k^p, \boldsymbol{\kappa}_k \right\}$ at time t_k should be computed according to the variables $\left\{ \boldsymbol{\sigma}_{k-1}, \mathbf{e}_{k-1}^p, \boldsymbol{\kappa}_{k-1} \right\}$ at the previous converged time t_{k-1} and the total applied strain, $\mathbf{e}_k$. This paper adopts an explicit time discretization method for Eqs. (40) and (42). Also, the yield function of Eq. (36) and the elastic equilibrium are expressed at the time t_k. The resulting set of algebraic equations at the time t_k is:

$$\begin{cases} \overline{\boldsymbol{\sigma}}_k = \mathbf{C}\left(\mathbf{e}_k - \mathbf{e}_k^p \right) \\ F\left(\overline{\boldsymbol{\sigma}}_k, \boldsymbol{\kappa}_k \right) = \dfrac{1}{1-\alpha} \left(\alpha \overline{I}_1 \left(\overline{\boldsymbol{\sigma}}_k \right) + \sqrt{3 \overline{J}_2 \left(\overline{\boldsymbol{\sigma}}_k \right)} + \beta \left\langle \hat{\overline{\sigma}}_{\max,k} \right\rangle - \gamma \left\langle -\hat{\overline{\sigma}}_{\max,k} \right\rangle \right) - \overline{C}_c \left(\kappa_{c,k} \right) = 0 \\ \mathbf{e}_k^p = \mathbf{e}_{k-1}^p + \dot{\lambda}_k \mathbf{m}\left(\overline{\boldsymbol{\sigma}}_{k-1} \right) \\ \boldsymbol{\kappa}_k = \boldsymbol{\kappa}_{k-1} + \dot{\lambda}_k \mathbf{H}\left(\hat{\overline{\boldsymbol{\sigma}}}_{k-1} \right) \end{cases} \tag{55}$$

Because the first, third and fourth equation of Eq. (55) are linear, they can be substituted into the second equation of Eq. (55) resulting in one equation, $F\left(\dot{\lambda}_k \right) = 0$, in one unknown, $\dot{\lambda}_k$. A Newton-Raphson solution strategy combining a secant method with bracketing is used to solve at each time instant t_k.

Because for elastic steps, $\dot{\lambda}_k = 0$, $\boldsymbol{\kappa}_k = \boldsymbol{\kappa}_{k-1}$ and $\mathbf{e}_k^p = \mathbf{e}_{k-1}^p$, the solution process first assumes that the entire increment, $\mathbf{e}_k - \mathbf{e}_{k-1}$ is elastic, and finds a trial stress as: $\overline{\boldsymbol{\sigma}}_k = \mathbf{C}\left(\mathbf{e}_k - \mathbf{e}_{k-1}^p \right)$. Then, this assumption is evaluated by calculating the yield function

$F\left(\bar{\boldsymbol{\sigma}}_k, \boldsymbol{\kappa}_k\right)$. If $F\left(\bar{\boldsymbol{\sigma}}_k, \boldsymbol{\kappa}_k\right) \le 0$, the assumption of elastic response is valid. If not, inelastic response occurs during that step and the nonlinear equation $F\left(\dot{\lambda}_k\right) = 0$ (representing the system of Eqs. (55)) has to be solved to determine $\dot{\lambda}_k$ and subsequently, $\boldsymbol{\kappa}_k$, $\mathbf{e}_k^p$, and $\bar{\boldsymbol{\sigma}}_k$. The damage factor, $D\left(\boldsymbol{\kappa}_k\right)$, is subsequently calculated from Eqs. (33), (34) and (35) and total stress is obtained as: $\boldsymbol{\sigma}_k = \left(1 - D\left(\boldsymbol{\kappa}_k\right)\right)\bar{\boldsymbol{\sigma}}_k$.

6. Assessment of Proposed Element Formulation

The proposed shear-enhanced GI element formulation and multiaxial concrete model were implemented in the structural analysis program OpenSees (McKenna et al. 2000). The formulation's performance in terms of response objectivity and accuracy is evaluated through examples and comparisons with experimental data as discussed in the following sections. The experimental data cover shear span-to-depth ratios, *a/d*, ranging from 2.1 to 7. The concrete material parameters adopted in all models are shown in . As indicated, some of these parameters are directly associated with experimentally measurable material properties, such as the concrete compressive strength, f'_c, and the concrete compressive strength at onset of inelastic response, f_{co}. The analysis run times for the shear-enhanced GI element varied depending on the number of IPs (NIPs), number of fibers per cross-section, and the values of the material parameters which affect convergence mainly in the post-peak range of the response. Overall, for all analyses presented, the run times varied between 3 and 8 hours on a desktop PC with Intel(R) Core(TM) i7-8700 CPU @ 3.20GHz 3.19 GHz.

Table 1 – Default material parameters used in numerical models

a_t	a_c	b_c	b_t	d_c	d_t	d_{ct}	K_c	f_{to}	f_{co}	f_{bo}	ψ	ρ
0.135	*	500	550	250	500	400	2/3	**	$0.25f'_c$	$1.15f_{co}$	$\pi/6$	0.1

* $a_c = \dfrac{2}{f_{c0}/f'_c}\left(\sqrt{1 - \dfrac{f_{c0}}{f'_c}} - 0.5\dfrac{f_{c0}}{f'_c} + 1\right) > 1$ ** $f_{t0} = 0.56\sqrt{f'_c}\ (\text{MPa}) = 6.7\sqrt{f'_c}\ (\text{psi})$

6.1. Response Objectivity

A major objective of the shear-enhanced GI element formulation is that it achieves response objectivity, i.e., convergence of global and local responses with progressive mesh refinement,

during shear damage and failure. In order to demonstrate this capability, the shear-flexure-critical column specimen R3 from Xiao et al. (1993), which was tested under lateral load and fixed top end rotation, is analyzed herein (Fig. 3). The shear span-to-depth ratio, *a/d*, for this column is about 2.1. The longitudinal and volumetric shear reinforcement ratios were 2.5% and 0.25%, respectively. The concrete compressive strength was 4.95 ksi. The yield strengths of the longitudinal bars and the stirrups were 68 ksi and 47 ksi, respectively. The vertical load, *P*, applied to the column was constant and equal to 114 kips.

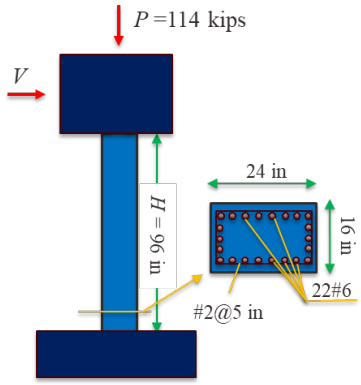

Fig. 3 – Details of column R3 tested by Xiao et al. (1993)

The entire column length is modeled via a single shear-enhance GI element. The composite Simpson's rule is adopted for the numerical integration of the strain-displacement equations (see second of Eqs. (20)). Different numbers of IPs (providing different levels of mesh refinement) are considered and each IP is represented through a higher-order fiber section. Each cross section is discretized into 8 by 12 fibers for the concrete and 22 separate fibers for the longitudinal steel. Concrete is modeled through the triaxial plasticity model discussed earlier. The response of the longitudinal reinforcement is represented via triaxial J2 plasticity material model, available in OpenSees. Bond-slip effects are accounted for according to Sharifi et al. (2020). The uniaxial material model representing the transverse reinforcement (used to enforce through-the-depth equilibrium) is Steel-02 with deterioration parameters, available in OpenSees.

The characteristic length, l_c, was taken to be 12 in. (i.e., half of the cross-section depth). Based on the previous studies with the GI formulation (Sideris and Salehi 2016; Salehi and Sideris 2017), a value of l_c between half and full cross-section depth has been found to provide a good agreement with the experimental data for ductile flexure-critical columns. In shear-critical elements, values of l_c between half and twice the cross-section depth may be reasonable, mainly because each single diagonal crack is expected to propagate within this range depending on the shear span to depth ratio.

The predicted lateral force vs. displacement responses are compared with the envelope of the (cyclic) test data in Fig. 4(a). It is observed that the element's pre-peak response remains almost unaffected by the NIPs. The post-peak responses converge with the number of IPs, which confirms the response objectivity of the proposed shear-enhanced GI element formulation. According to Fig. 4(b), an $l_c/\Delta x$ ratio greater than 3 is found to ensure the convergence of the force-displacement response.

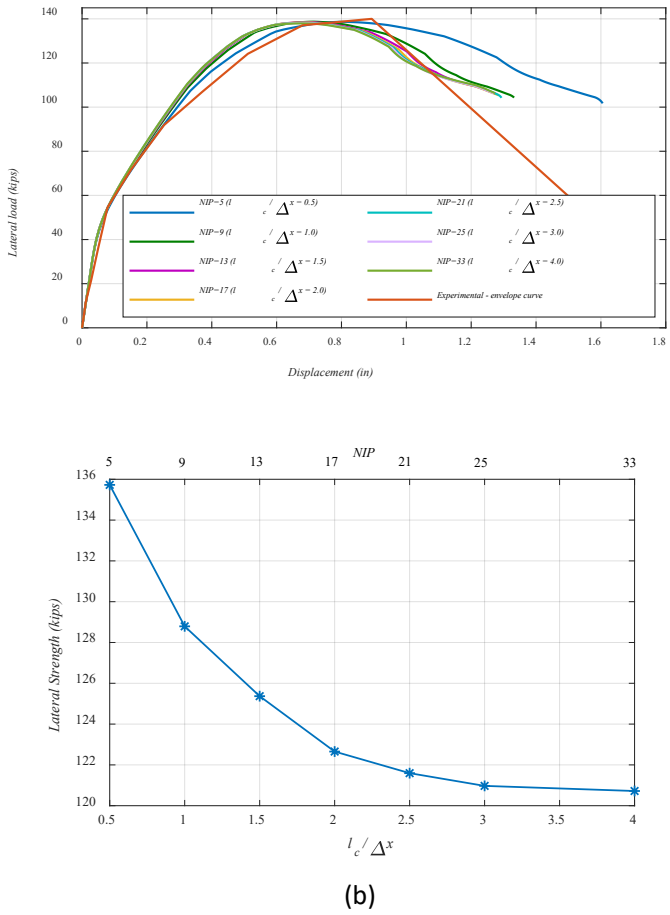

(b)

Fig. 4 – Response objectivity: (a) force-displacement responses; (b) variation of strength with $l_c/\Delta x$ at a lateral displacement of 1 in.

The predicted distributions of macroscopic shear strain (on the reference axis, i.e., γ_{xyo}) and curvature at 1 in. of lateral displacement as well as the corresponding variations of peak shear strain and curvature with $l_c/\Delta x$ are shown in Fig. 5. As expected, both the peak shear strains and curvatures are predicted to occur at the column ends (Fig. 5(a,c)), where the ultimate failure occurred during the experiment (Xiao et al. 1993). Similar to the force-displacement responses (Fig. 4), the predicted macroscopic section strains appear to converge as $l_c/\Delta x$ exceeds 3 (per Fig. 5 (b,d)).

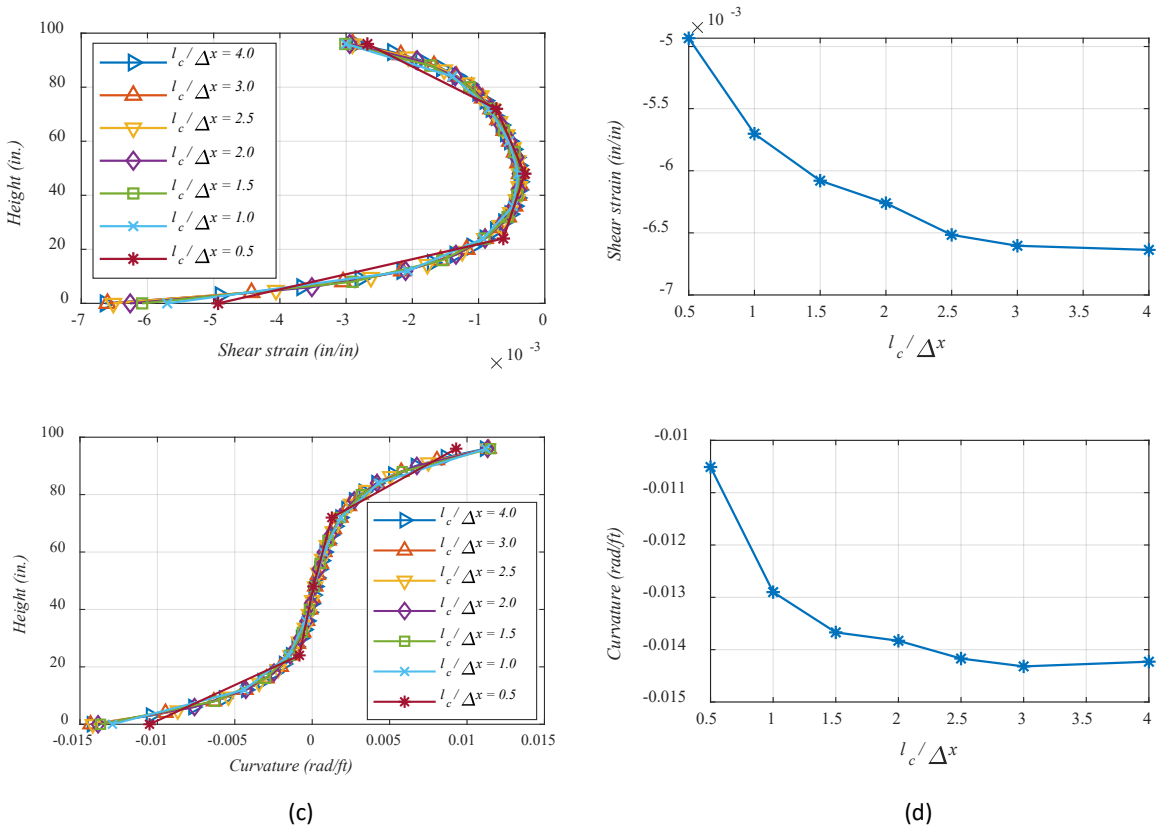

Fig. 5 – Response objectivity – Macroscopic section strain distributions at lateral displacement of 1.0 in.: (a) shear strain; (c) curvature; variations of maximum section strains with $l_c/\Delta x$ at lateral displacement of 1.0 in.: (b) shear strain; (d) curvature

6.2. Effect of Characteristic Length

The effect of characteristic length, l_c, on the response of the shear-enhanced GI FB element formulation is examined using the column model from the previous example. The lateral load vs. displacement response predictions for three different values of l_c, namely, half, one-, and two-times cross-section depths, are shown in Fig. 6(a). In each case, the number of IPs is selected to satisfy $l_c/\Delta x \geq 2.5$ to ensure mesh-independent responses, i.e., 7 IPs, 11 IPs, and 21 IPs for l_c equal to half, one-, and two-times cross-section depths, h_{col}, respectively. It is observed that larger values of l_c increase the lateral displacement corresponding to the peak column strength (i.e., delay the onset of softening) and reduce the rate of the post-peak strength deterioration. As seen in the macroscopic shear strain and curvature distributions (Fig. 6(b,c)), the delay in softening is caused by the spread of plasticity/damage over a larger length as l_c increases. Moreover, when compared to the experimental response, it is confirmed that an l_c value around half a column depth leads to a reasonably accurate model prediction.

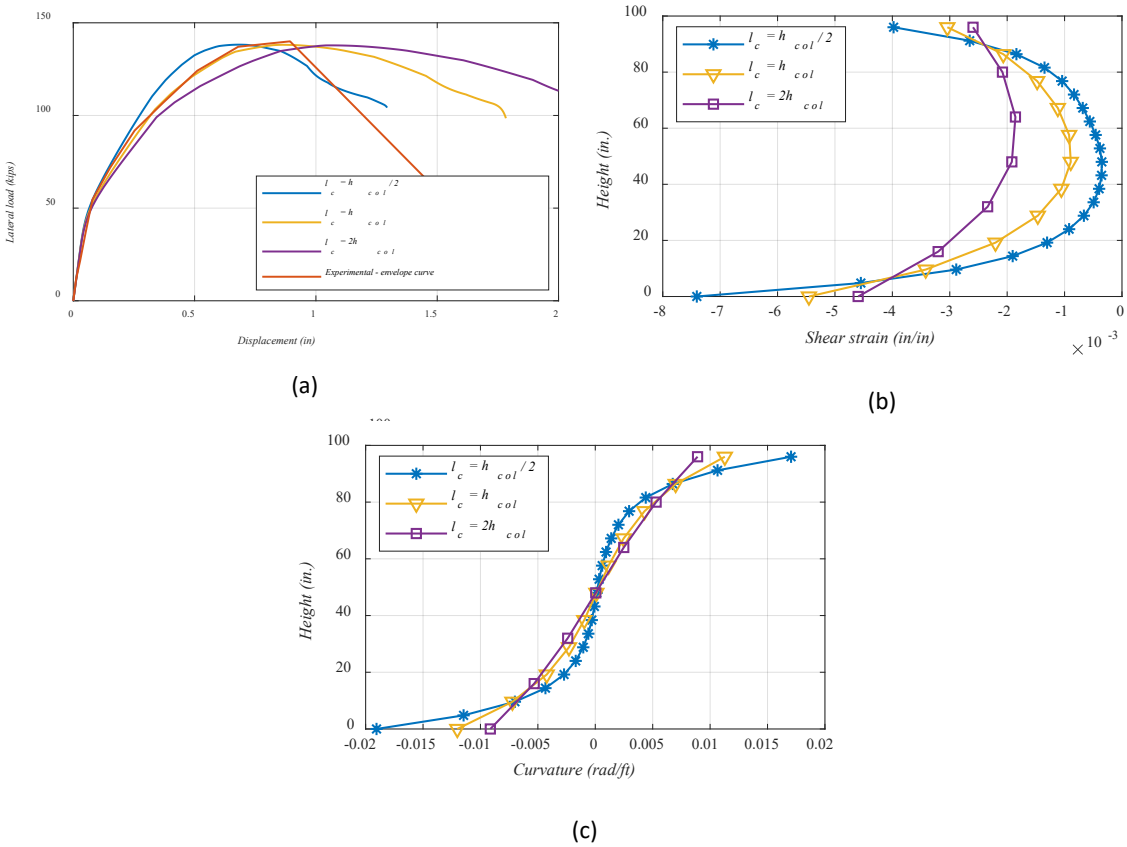

Fig. 6 – Effect of characteristic length: (a) force-displacement responses; macroscopic section strain distributions at lateral displacement of 1.3 in.: (b) shear strain; (c) curvature

6.3. Comparison with Original GI Element

The lateral load-displacement response predictions of the original and shear-enhanced GI elements are compared using the column adopted in the previous two sections (see Fig. 3). In both models, the characteristic length, l_c, is selected to be 12 in. (half the cross-section depth) and the number of IPs is taken as 21 to ensure response objectivity ($l_c/\Delta x \geq 2.5$). In the fiber sections of the original GI element, the response of the concrete material and the longitudinal steel are modeled by the Mander's material model (Mander et al. 1988) and Giuffre-Menegotto-Pinto model (Giuffrè and Pinto 1970), respectively, which are available in OpenSees.

The force vs. displacement responses and macroscopic section strain distributions of the two models are compared with each other and the experimental data in Fig. 7. The shear-enhanced GI element predicts a much lower strength and rapid post-peak degradation (Fig. 7 (a)), which are driven by shear damage. On the contrary, the original GI predicts a significantly more ductile response that is driven by flexural failure, which would only occur if the RC

member was capacity-protected against shear failure. In fact, while both the original and the shear-enhanced GI element formulation predict similar curvature distributions over the member (Fig. 7 (b)), the shear-enhanced GI element predicts large, nonlinear shear strain distributions (Fig. 7 (c)), which are indicative of its capability to predict shear failures. However, the original GI predicts very small, linearly distributed, shear strains (Fig. 7 (c)). This is because it adopts the (linear) cross-section kinematics of Timoshenko beams and uniaxial stress vs. strain constitutive laws normal to the cross-section plane that are decoupled from the shear stress vs. shear strain relations, which are often taken to be linear. On the contrary, the shear-enhanced GI formulation adopts cubic cross-section kinematics and 3D constitutive relations that can describe the coupled effect of normal and shear stresses and the resulting higher order field.

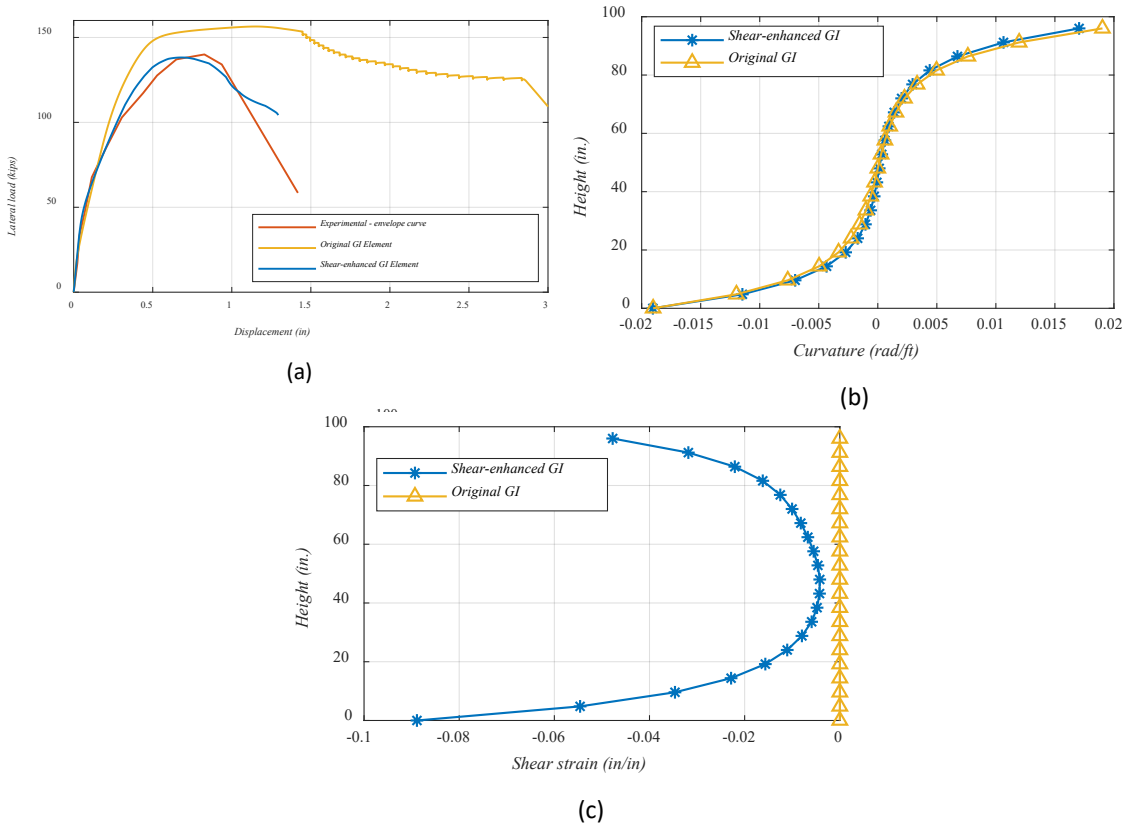

Fig. 7 – Comparison of responses with original GI element: (a) force-displacement response; (b) macroscopic section shear strain distribution at a lateral displacement of 1.3 in.; (c) macroscopic section curvature distribution at a lateral displacement of 1.3 in.

6.4. Comparison with Experimental Data

The performance of the shear-enhanced GI FB element formulation is further evaluated by simulating eleven different RC members, namely nine beams (Vecchio and Shim 2004) and

two columns (Prakash et al. 2012; Pan and Li 2013), from three experimental studies available in the literature.

6.4.1. Shear-critical Reinforced Concrete Beams

The cross-section dimensions and reinforcement details of the examined beams (Vecchio and Shim 2004) are provided in Fig. 8, , and . As shown in Fig. 8, the beam series A, B, and C have different cross-section dimensions. Each series consists of three sub-series, namely 1, 2 and 3. Sub-series 1 and 2 had shear span-to-depth ratios, *a/d*, of 4 and 5, respectively, and exhibited shear failure starting with diagonal-tension cracking and later also exhibiting splitting in the compression zone. Sub-series 3 had *a/d* of 7 and exhibited flexural-compression failures with less shear deformations, but still showing diagonal cracking. The concrete compressive strengths were 22.6, 25.9 and 43.5 MPa for sub-series 1, 2 and 3, respectively. The yield strengths of the longitudinal steel bars were 315, 440, 445 and 436 MPa for M10, M25 in sub-series 2, M25 in sub-series 1 & 3, and M30, respectively. The yield strength of the stirrups was 600 MPa.

Considering the geometry and loading symmetry as provided in Fig. 9, only half of the length of each beams is modeled via a single shear-enhanced GI FB element with pinned-fixed BCs. The characteristic length, l_c, is selected to equal each beam's cross-section depth and the number of IPs is chosen such that $l_c/\Delta x \geq 2.5$ to ensure response objectivity. Each cross section is discretized into 8 by 14 fibers for the concrete materials, and additional separate fibers are introduced for the longitudinal steel bars. The concrete is modeled by the 3D concrete damage plasticity model discussed earlier with the material parameters of . The responses of the transverse and longitudinal reinforcement are represented via the Giuffré-Menegotto-Pinto uniaxial material model (Giuffrè and Pinto 1970) and triaxial J2 plasticity material model available in OpenSees, respectively. No bond-slip effect is considered in the beam models which was the case in the experimental tests. Monotonic loading was applied to failure.

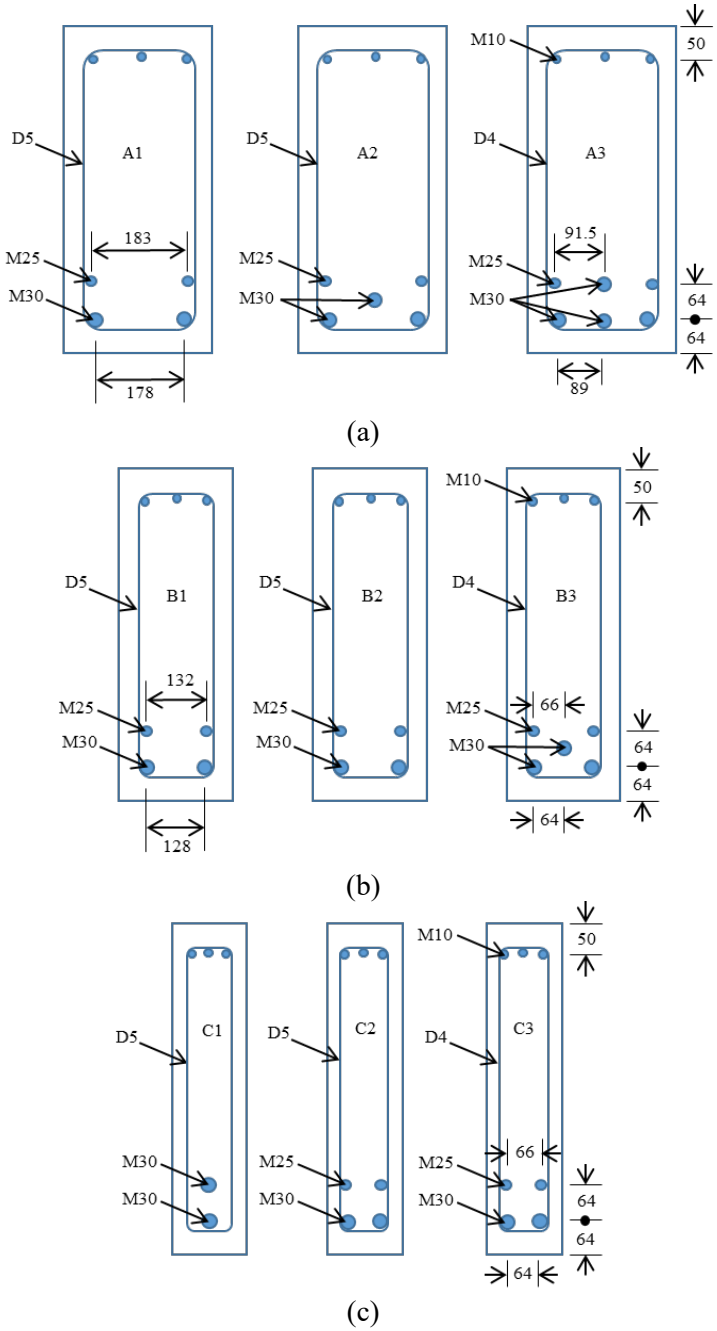

Fig. 8 – Details of examined RC beams: (a) series A; (b) series B; (c) series C (Vecchio and Shim 2004)

Table 2 – Cross-section details of Toronto beams (Vecchio and Shim 2004)

Beam ID	*b* (mm)	*h* (mm)	*d* (mm)	*L* (mm)	Span (mm)	*a/d*	Concrete strength (MPa)	Bottom steel	Top steel	Stirrups
VS-A1	305	552	457	4100	3660	4	22.6	2M30, 2M25	3M10	D5@210
VS-A2	305	552	457	5010	4570	5	25.9	3M30, 2M25	3M10	D5@210
VS-A3	305	552	457	6840	6400	7	43.5	4M30, 2M25	3M10	D4@168
VS-B1	229	552	457	4100	3660	4	22.6	2M30, 2M25	3M10	D5@190

VS-B2	229	552	457	5010	4570	5	25.9	2M30, 2M25	3M10	D5@190
VS-B3	229	552	457	6840	6400	7	43.5	3M30, 2M25	3M10	D4@152
VS-C1	152	552	457	4100	3660	4	22.6	2M30	3M10	D5@210
VS-C2	152	552	457	5010	4570	5	25.9	2M30, 2M25	3M10	D5@210
VS-C3	152	552	457	6840	6400	7	43.5	2M30, 2M25	3M10	D4@168

Table 3 – Steel material properties of Toronto beams (Vecchio and Shim 2004)

Bar size	Diameter (mm)	Area (mm^2)	f_y (MPa)	f_u (MPa)
M10	11.3	100	315	460
M25[a]	25.2	500	440	615
M25[b]	25.2	500	445	680
M30	29.9	700	436	700
D4	3.7	25.7	600	651
D5	6.4	32.2	600	649

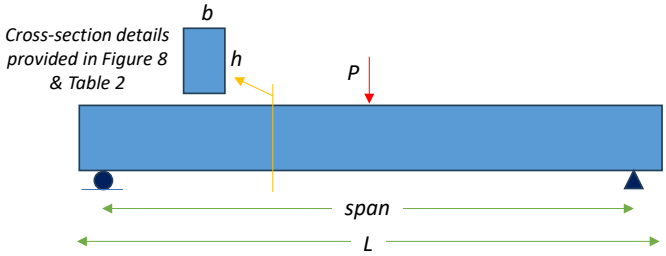

Fig. 9 – Loading and boundary conditions in examined beams

The response predictions of the shear-enhanced GI FB element formulation with and without the through-the-depth stress equilibrium are compared with the experimental data (Vecchio and Shim 2004) in Fig. 10 and Fig. 11 for the shear-dominant beams and the flexural compression beams, respectively. As shown in Fig. 10, incorporation of the through-the-depth equilibrium negligibility affects the pre-peak range, but it significantly affects the post-peak range by predicting slower softening that better aligns with the experimental data. This observation also aligns with the findings of Vecchio and Shim (2004) who noted the importance of simulating out-of-plane confinement effects in predicting the response of such beams. The shear-enhanced GI element formulation predicts the lateral strength very accurately with a mean strength prediction error of about 2.78% for the selected specimens as shown in . The shear-enhanced GI element formulation also captures the initial stiffness and the peak strength reasonably well. However, a later change in the stiffness in the pre-peak portion of the curve, which may be associated with initial cracking, is not accurately captured for the shear-dominant members of sub-series 1 and 2 (see Fig. 10). Analyses conducted with l_c equal to the

cross-section height ($l_c = h$) and twice the cross-section height ($l_c = 2h$) – see Fig. 10 (c), (d) and (e) – did not affect the pre-peak range predictions, however the case of $l_c = 2h$ provided more ductile post-peak responses that better followed the experimental data. For these specimens, the selected l_c (= $2h$) was also compatible with the average inclination of the shear cracks. Fine-tuning in the material parameters of , such as b_c and b_t, which affect the pre-peak response could improve the pre-peak response prediction, but such a fine-tuning search would be beyond the scope of this work.

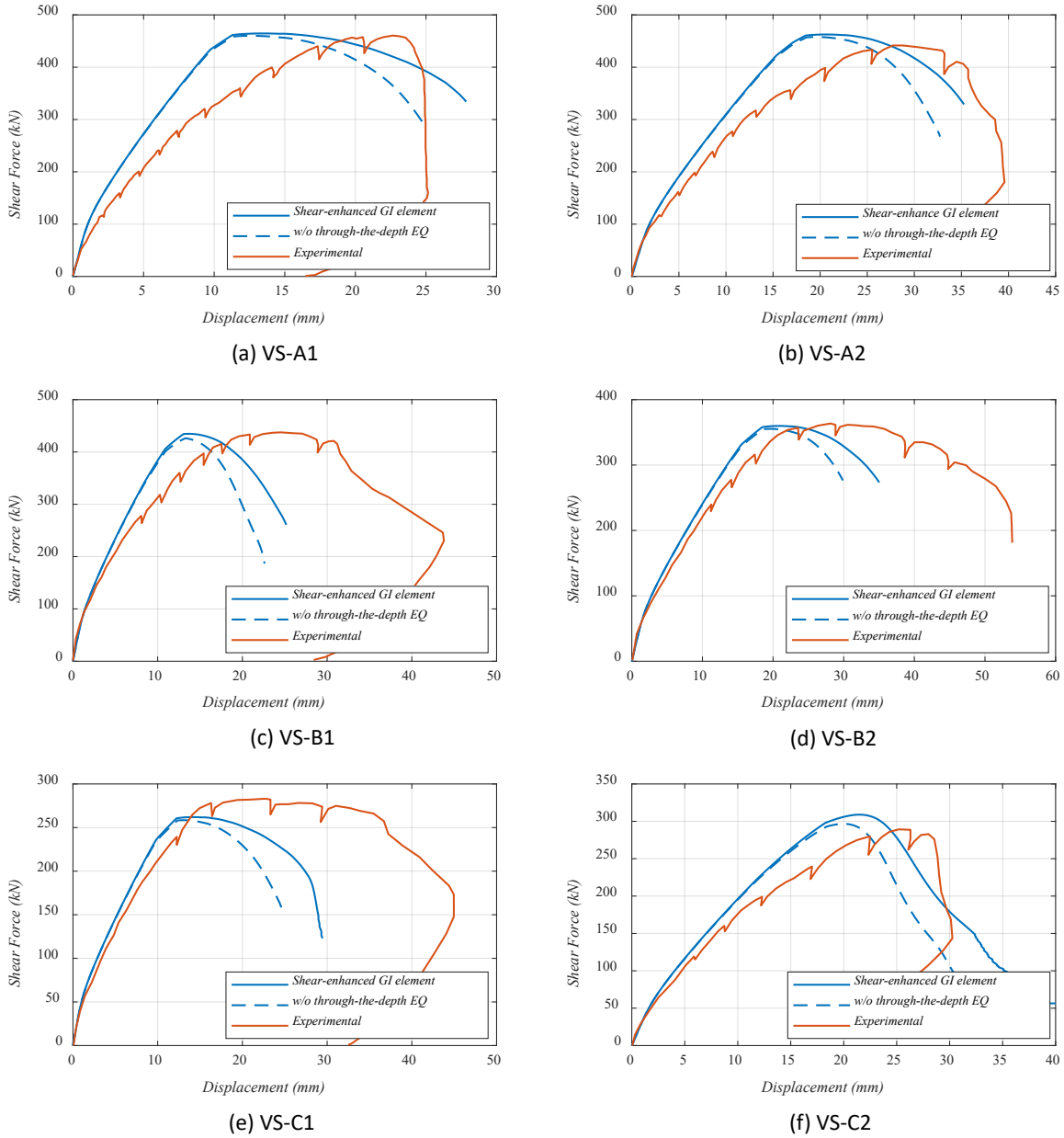

Fig. 10 – Comparison of force-displacement response predictions of proposed element formulation with experimental data for shear-dominant beams

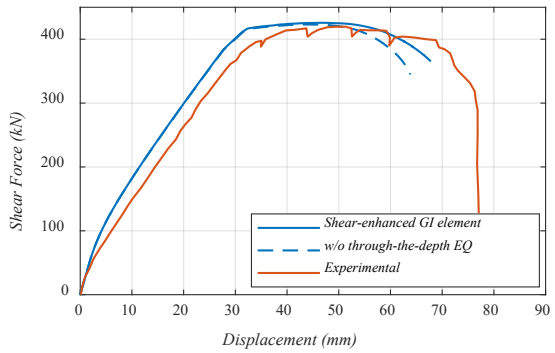

(a) VS-A3

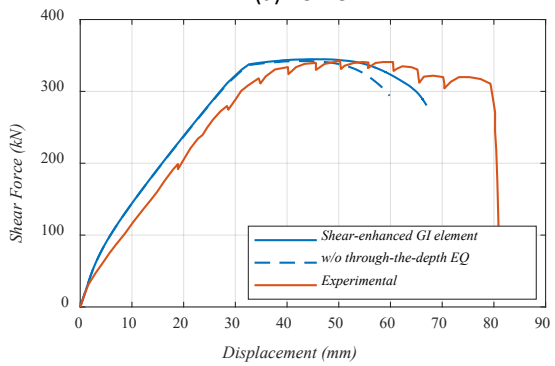

(b) VS-B3

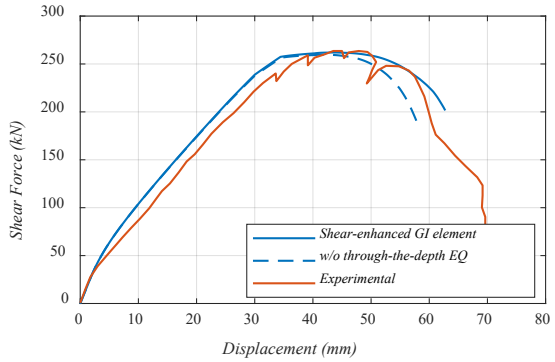

(c) VS-C3

Fig. 11 – Comparison of force-displacement response predictions of proposed element formulation with experimental data for flexural compression beams

Table 4 – Comparison of the maximum load predictions of the shear-enhanced GI element with experimental data

Beam ID	Maximum Vertical Load (kN)		δ (%)
	Experiment, P_{Exp}	Shear-enhanced GI Element, P_{SGI}	
A1	459	464.5	1.20
A2	439	462.6	5.38
A3	420	425.7	1.36
B1	434	434.7	0.16
B2	365	359.8	1.42
B3	342	344.7	0.79
C1	282	262	7.09

C2	290	308.9	6.52
C3	265	262	1.13
Mean			2.78
Median			1.36

6.4.2. Shear-critical Reinforced Concrete Columns

The properties of the examined columns are shown in Fig. 12 and . For each analysis, the entire column is modeled via a single shear-enhanced GI element with the composite Simpson's integration rule. The selected characteristic lengths, l_c, and the shear span-to-depth ratio, a/d, for the different columns are listed in , and number of IPs are considered for each element such that $l_c/\Delta x \geq 2.5$ to ensure mesh-converged responses. Each cross section is discretized into 12 by 16 fibers for concrete and separate fibers to represent longitudinal steel. The concrete is represented by the 3D concrete damage plasticity model discussed earlier. The responses of the transverse and longitudinal reinforcement are represented via the Giuffré-Menegotto-Pinto uniaxial material model (Giuffrè and Pinto 1970) and triaxial J2 plasticity material model available in OpenSees, respectively. The bond-slip effects are modeled per Sharifi et al. (2020).

Table 5 – Details of selected columns

Test	Specimen ID	B.C.		Material properties			P	l_c
				f'_c	f_y	f_{ys}		
Pan & Li (2013)	SC-2.4-0.3	Fixed-Fixed		49.3 MPa	409 MPa	392.6 MPa	$0.3f'_cA_g$	350 mm
Prakash et al. (2012)	H/B(6)-T/M(0)	Cantilever		36.3 MPa	512 MPa	454 MPa	$0.07f'_cA_g$	560 mm

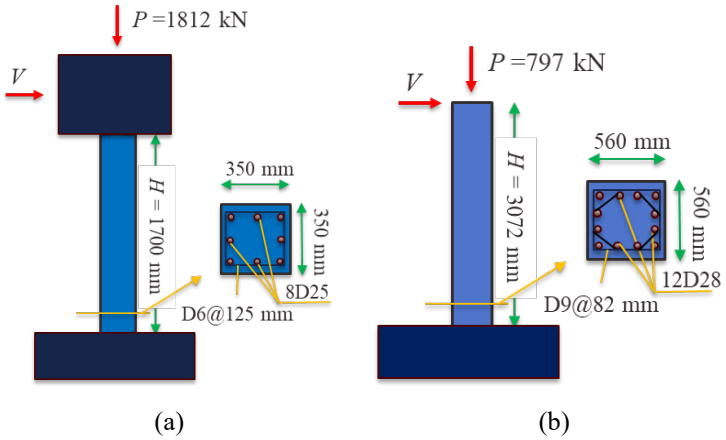

(a) (b)

Fig. 12 – Details of examined columns: (a) Pan & Li (2013); (b) Prakash et al. (2012)

The pushover responses predicted from the shear-enhanced GI element formulation are compared with the envelope curves of the experimental cyclic response from both tests in Fig.

13. The three different analysis strategies were adopted, namely: (1) including both through-the-depth equilibrium and bond-slip effects, (2) disregarding through-the-depth equilibrium and calculating the lateral strains through Poisson's ratio ($\varepsilon_{yy} = \varepsilon_{zz} = -\nu\varepsilon_{xx}$) while keeping bond-slip effects, and (3) disregarding bond-slip effects while keeping through-the-depth equilibrium. As expected, considering the bond-slip effects generally improves the model response predictions – especially, in terms of the pre-peak stiffness. Also, the models with no through-the-depth force equilibrium, in which lateral strains were calculated from Poisson's ratio relation, exhibit less ductility due to their inability to capture out-of-plane confinement effects. The shear-enhanced GI elements with both bond-slip and through-the-depth equilibrium not only closely captures the overall shapes of the force-displacement responses obtained from the experiments, but also predict the lateral strengths of the columns with only about 3% error.

It is noted that while the actual lateral loading histories were cyclic (for this section and for Section 6.1), and despite the fact that the shear GI formulation can inherently account for cyclic loading through the use of a concrete constitutive model that belongs to the family of classical incremental plasticity models, the analyses conducted herein for the RC columns were selected to be monotonic. This is because simulating the deterioration from repeated cyclic loading at various amplitudes requires more complex definitions for κ_c and κ_t. The adopted definition of Eqs. (42) to (44) implies that κ_c and κ_t represent accumulated plastic traveling in compression and tension, respectively. While this definition (or similar definitions, e.g. Lee and Fenves (1998)) has been found to satisfactorily predict deterioration under uniaxial monotonic loading or simple uniaxial cyclic loading, the material model in the present study is subjected to complex triaxial loading due to the through-the-depth equilibrium, for which this definition of κ_c and κ_t may not be suitable. For example, a recent study by McKee et al. (2023) on steel rebar showed that strength deterioration and damage depend both on the accumulated plastic traveling and the strain magnitude at which the traveling takes place, showing that cycles at larger strains may be more damaging than cycles at lower strains, and demonstrating the need for more complex definitions of damage parameters. Exploring definitions of κ_c and κ_t that can account for similar observations in concrete, while being of value, are deemed to be beyond the scope of this paper.

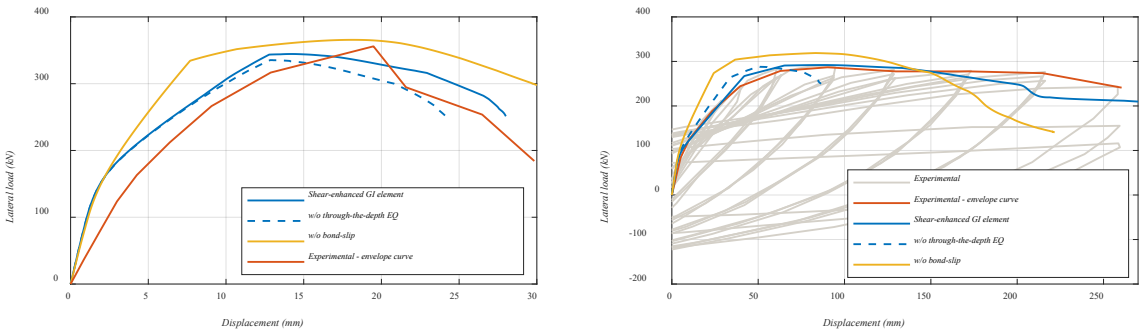

(a) (b)

Fig. 13 – Comparison of force-displacement response predictions with experimental data: (a) Pan & Li (2013); (b) Prakash et al. (2012)

7. Summary and Conclusions

This paper extends a previously developed gradient inelastic (GI) force-based (FB) beam-column element formulation capable of capturing axial-flexural interactions and predicting flexural failures to account for axial-flexural-shear interactions in order to predict shear failures in RC members. This is achieved by incorporating (*i*) higher-order cross-section kinematics to describe higher-order transverse deformation profiles, (*ii*) cross-sectional through-the-depth equilibrium to predict normal strain distributions in the transverse directions and to compensate for confinement effects, and (*iii*) 3D concrete constitutive relations to simulate triaxial stress/strain interactions. The higher-order cross-section kinematics are determined through satisfaction of cross-section boundary conditions (BCs) and, as a result, do not introduce additional element degrees of freedom. The adopted 3D concrete constitutive relations are based on the plastic damage model of Lee and Fenves (1998), which, amongst other modifications, it is also modified herein to include the effect of compression softening due to the presence of reinforcement. To eliminate strain localization phenomena, new gradient nonlocality relationships are introduced, in addition to those of the original GI FB formulation. The proposed element formulation is implemented in the OpenSees structural analysis software (McKenna et al. 2000). Some additional observations include:

- The shear-enhanced GI element formulation was found to eliminate strain localization phenomena during softening and provide mesh-convergent responses. For the analyses performed, convergence was achieved for $l_c/\Delta x$ of 2.5 to 3 or larger.
- Incorporation of the *through-the-depth* equilibrium led to more ductile shear-dominant post-peak responses, which were found to better match the experimental data.

- Comparisons with experimental data showed that the original GI element (without shear effects) overestimated the peak lateral strength of shear-critical RC members, whereas the shear-enhanced GI element was able to predict such strength with less than 3% error (on average) based on comparisons with test data from 12 different RC members.
- While the shear-enhanced GI element provide similar accuracy in predicting the strength in RC beams and columns, it provided more accurate predictions of the post-peak response of columns compared to the post-peak response of beams. Use of more accurate values of the characteristic length, l_c, improved the predictions for shear-dominant columns.
- While the shear-enhanced GI formulation inherently accounts for arbitrary loading conditions, all analyses focused on monotonic loading. Refinements of the material model, most likely with respect to the damage parameters and damage factors, are needed through future research to better describe material degradation with repeated loading cycles at varying strain amplitudes and under triaxial conditions.

The shear-enhanced GI element formulation could contribute to the analysis of non-ductile RC framed structures in the U.S. and worldwide. Such structures often pose an imminent threat to catastrophic failure due to earthquakes and/or other natural hazards. While this study focused on two-dimensional loading conditions, future research may extend this work to account for biaxial bending and torsional effects resulting from complex three-dimensional loading conditions.

Acknowledgements

Partial financial support to the third author has been provided by the National Science Foundation (NSF) under grant #2032352. This support is gratefully acknowledged. The findings presented herein are those of the authors and do not necessarily reflect the views of the NSF.

Data Availability

Some or all data, models, or code that support the findings of this study are available from the corresponding author upon reasonable request.

References

Aghajani Delavar, M., Bargi, K. (2018). "Prediction of Local Seismic Damage in Jacket-type Offshore Platforms." *AUT Journal of Civil Engineering*, 2(2): 241-250.

Aghajani Delavar, M., Bargi, K. (2020). "Seismic Response Control of Offshore Platforms Equipped with Optimum Localization of SMA." *engrXiv*, DOI: 10.31224/osf.io/8y9d5.

Almeida, J., Das, S., Pinho, R. (2012). "Adaptive force-based frame element for regularized softening response." *Computers & Structures*, 102: 1-13.

Bairan, J. M., Mari, A. R. (2007). "Multiaxial-coupled analysis of RC cross-sections subjected to combined forces." *Engineering structures*, 29(8): 1722-1738.

Bentz, E. C. (2000). *Sectional analysis of reinforced concrete members*, University of Toronto Toronto. ISBN 0612498409.

Bhimaraddi, A., Chandrashekhara, K. (1993). "Observations on higher-order beam theory." *Journal of Aerospace Engineering*, 6(4): 408-413.

Ceresa, P., Petrini, L., Pinho, R. (2007). "Flexure-shear fiber beam-column elements for modeling frame structures under seismic loading—state of the art." *Journal of Earthquake Engineering*, 11(S1): 46-88.

Ceresa, P., Petrini, L., Pinho, R., Sousa, R. (2009). "A fibre flexure‐shear model for seismic analysis of RC ‐ framed structures." *Earthquake Engineering & Structural Dynamics*, 38(5): 565-586.

Coleman, J., Spacone, E. (2001). "Localization issues in force-based frame elements." *Journal of Structural Engineering*, 127(11): 1257-1265.

Correia, A. A., Almeida, J. P., Pinho, R. (2015). "Force-based higher-order beam element with flexural–shear–torsional interaction in 3D frames. Part I: Theory." *Engineering Structures*, 89: 204-217.

Cowper, G. (1966). "The shear coefficient in Timoshenko's beam theory."

D'Ambrisi, A., Filippou, F. C. (1999). "Modeling of cyclic shear behavior in RC members." *Journal of Structural Engineering*, 125(10): 1143-1150.

Di Re, P., Addessi, D., Filippou, F. C. (2018). "Mixed 3D beam element with damage plasticity for the analysis of RC members under warping torsion." *Journal of Structural Engineering*, 144(6): 04018064.

Feng, D.-C., Ren, X., Li, J. (2016). "Implicit gradient delocalization method for force-based frame element." *Journal of Structural Engineering*, 142(2): 04015122.

Feng, D.-C., Ren, X.-D., Li, J. (2018). "Softened damage-plasticity model for analysis of cracked reinforced concrete structures." *Journal of Structural Engineering*, 144(6): 04018044.

Feng, D.-C., Wu, G., Ning, C.-L. (2019). "A regularized force-based Timoshenko fiber element including flexure-shear interaction for cyclic analysis of RC structures." *International Journal of Mechanical Sciences*, 160: 59-74.

Feng, D. C., Ren, X. (2021). "Implicit gradient ‐ enhanced force ‐ based Timoshenko fiber element formulation for reinforced concrete structures." *International Journal for Numerical Methods in Engineering*, 122(2): 325-347.

Filippou, F. C., D'ambrisi, A., Issa, A. (1992). *Nonlinear static and dynamic analysis of reinforced concrete subassemblages*, Earthquake Engineering Research Center, College of Engineering, University …,

Filippou, F. C., Saritas, A. (2006). "A beam finite element for shear-critical RC beams." *ACI Special Publications*, 237: 295.

Floegl, H., Mang, H. A. (1982). "Tension stiffening concept based on bond slip." *Journal of the Structural Division*, 108(12): 2681-2701.

Garcia, J. M. B., Bernat, A. R. M. (2006). "Coupled model for the non-linear analysis of anisotropic sections subjected to general 3D loading. Part 1: Theoretical formulation." *Computers & structures*, 84(31-32): 2254-2263.

Garcia, J. M. B., Mari, A. R. (2006). "Coupled model for the nonlinear analysis of sections made of anisotropic materials, subjected to general 3D loading. Part 2: Implementation and validation." *Computers & structures*, 84(31-32): 2264-2276.

Ghugal, Y. M., Sharma, R. (2009). "A hyperbolic shear deformation theory for flexure and vibration of thick isotropic beams." *International Journal of Computational Methods*, 6(04): 585-604.

Giuffrè, A., Pinto, P. E. (1970). "Il comportamento del cemento armato per sollecitazioni cicliche di forte intensità." *Giornale del Genio Civile*, 5(1): 391-408.

Haselton, C. B. (2007). *Assessing seismic collapse safety of modern reinforced concrete moment frame buildings*. ISBN 0542983451.

Haselton, C. B., Liel, A. B., Taylor-Lange, S. C., Deierlein, G. G. (2016). "Calibration of model to simulate response of reinforced concrete beam-columns to collapse." *ACI Structural Journal*, 113(6).

Hellesland, J., Scordelis, A. "Analysis of RC bridge columns under imposed deformations." *Proc., IABSE colloquium*, Delft the Netherlands, 545-559.

Hippola, H., Wijesundara, K., Nascimbene, R. (2022). "Response of shear critical reinforced concrete frames and walls under monotonic loading." *Engineering Structures*, 251: 113483.

Hsu, T. T. (1988). "Softened truss model theory for shear and torsion." *Structural Journal*, 85(6): 624-635.

Jensen, J. J. (1983). "On the shear coefficient in Timoshenko's beam theory." *Journal of Sound and Vibration*, 87(4): 621-635.

Jiang, H., Kurama, Y. C. (2010). "Analytical Modeling of Medium-Rise Reinforced Concrete Shear Walls." *ACI Structural Journal*, 107(4).

Ju, J. (1989). "On energy-based coupled elastoplastic damage theories: constitutive modeling and computational aspects." *International Journal of Solids and structures*, 25(7): 803-833.

Kagermanov, A., Ceresa, P. (2018). "3D fiber-based frame element with multiaxial stress interaction for RC structures." *Advances in Civil Engineering*, 2018.

Kaneko, T. (1975). "On Timoshenko's correction for shear in vibrating beams." *Journal of Physics D: Applied Physics*, 8(16): 1927.

Kenawy, M., Kunnath, S., Kolwankar, S., Kanvinde, A. (2018). "Fiber-Based Nonlocal Formulation for Simulating Softening in Reinforced Concrete Beam-Columns." *Journal of Structural Engineering*, 144(12), DOI: Artn 04018217

10.1061/(Asce)St.1943-541x.0002218.

Kenawy, M., Kunnath, S., Kolwankar, S., Kanvinde, A. (2020). "Concrete uniaxial nonlocal damage-plasticity model for simulating post-peak response of reinforced concrete beam-columns under cyclic loading." *Journal of structural engineering*, 146(5): 04020052.

Khaloo, A. R., Tariverdilo, S. (2002). "Localization analysis of reinforced concrete members with softening behavior." *J Struct Eng-Asce*, 128(9): 1148-1157.

Kunnath, S. K., Reinhorn, A. M., Park, Y. J. (1990). "Analytical modeling of inelastic seismic response of R/C structures." *Journal of Structural Engineering*, 116(4): 996-1017.

LeBorgne, M., Ghannoum, W. (2014). "Analytical element for simulating lateral-strength degradation in reinforced concrete columns and other frame members." *Journal of Structural Engineering*, 140(7): 04014038.

Lee, D. H., Kim, D., Park, T. (2009). "Earthquake response analysis of RC bridges using simplified modeling approaches." *Journal of sound and vibration*, 324(3-5): 640-665.

Lee, J., Fenves, G. L. (1998). "Plastic-Damage Model for Cyclic Loading of Concrete Structures." *Journal of Engineering Mechanics*, 124(8): 892-900.

Levinson, M. (1981). "A new rectangular beam theory." *Journal of Sound and vibration*, 74(1): 81-87.
Li, Z.-X., Gao, Y., Zhao, Q. (2016). "A 3D flexure–shear fiber element for modeling the seismic behavior of reinforced concrete columns." *Engineering Structures*, 117: 372-383.
Limkatanyu, S., Spacone, E. (2002). "Reinforced concrete frame element with bond interfaces. I: Displacement-based, force-based, and mixed formulations." *Journal of Structural Engineering*, 128(3): 346-355.
Lodhi, M., Sezen, H. (2012). "Estimation of monotonic behavior of reinforced concrete columns considering shear‐flexure‐axial load interaction." *Earthquake engineering & structural dynamics*, 41(15): 2159-2175.
Lubliner, J., Oliver, J., Oller, S., Onate, E. (1989). "A plastic-damage model for concrete." *International Journal of solids and structures*, 25(3): 299-326.
Mander, J. B., Priestley, M. J., Park, R. (1988). "Theoretical stress-strain model for confined concrete." *Journal of structural engineering*, 114(8): 1804-1826.
Marini, A., Spacone, E. (2006). "Analysis of reinforced concrete elements including shear effects." *ACI Structural Journal*, 103(5): 645.
Massicotte, B., Elwi, A. E., MacGregor, J. G. (1990). "Tension-stiffening model for planar reinforced concrete members." *Journal of Structural Engineering*, 116(11): 3039-3058.
McKee, C. D., Sideris, P., Hubler, M. (2023). "A Macromechanical Constitutive Model for Rebar Buckling." *Journal of Structural Engineering* 149(8), DOI: 10.1061/JSENDH.STENG-11349.
McKenna, F., Fenves, G. L., Scott, M. H. (2000). "Open system for earthquake engineering simulation." *University of California, Berkeley, CA*.
Mergos, P., Kappos, A. (2008). "A distributed shear and flexural flexibility model with shear–flexure interaction for R/C members subjected to seismic loading." *Earthquake Engineering & Structural Dynamics*, 37(12): 1349-1370.
Mergos, P., Beyer, K. (2014). "Modelling shear–flexure interaction in equivalent frame models of slender reinforced concrete walls." *The Structural Design of Tall and Special Buildings*, 23(15): 1171-1189.
Mindlin, R., Deresiewicz, H. (1953). "Timoshenko's shear coefficient for flexural vibrations of beams." COLUMBIA UNIV NEW YORK,
Mohr, S., Bairán, J. M., Marí, A. R. (2010). "A frame element model for the analysis of reinforced concrete structures under shear and bending." *Engineering structures*, 32(12): 3936-3954.
Mullapudi, T., Ayoub, A. (2012). "Analysis of reinforced concrete columns subjected to combined axial, flexure, shear, and torsional loads." *Journal of Structural Engineering*, 139(4): 561-573.
Neuenhofer, A., Filippou, F. C. (1997). "Evaluation of nonlinear frame finite-element models." *Journal of structural engineering*, 123(7): 958-966.
Nguyen, T.-A., Nguyen, Q.-H., Somja, H. (2019). "An enhanced finite element model for reinforced concrete members under torsion with consistent material parameters." *Finite Elements in Analysis and Design*, 167: 103323.
Nikoukalam, M. T., Sideris, P. (2019). "Nonlocal Hardening-Damage Beam Model and its Application to a Force-based Element Formulation." *ASCE Journal of Engineering Mechanics (Special Collection on Recent Advances in Computational Methods in Engineering Mechanics)*, 145(10), DOI: https://doi.org/10.1061/(ASCE)EM.1943-7889.0001659.
Pan, Z., Li, B. (2013). "Truss-arch model for shear strength of shear-critical reinforced concrete columns." *Journal of Structural Engineering*, 139(4): 548-560.

Petrangeli, M., Pinto, P. E., Ciampi, V. (1999). "Fiber element for cyclic bending and shear of RC structures. I: Theory." *Journal of Engineering Mechanics*, 125(9): 994-1001.
Prakash, S., Li, Q., Belarbi, A. (2012). "Behavior of circular and square reinforced concrete bridge columns under combined loading including torsion." *ACI Structural Journal*, 109(3): 317-328.
Priestley, M. (1997). "Displacement-based seismic assessment of reinforced concrete buildings." *Journal of earthquake engineering*, 1(01): 157-192.
Rajapakse, R., Wijesundara, K., Nascimbene, R., Bandara, C., Dissanayake, R. (2019). "Accounting axial-moment-shear interaction for force-based fiber modeling of RC frames." *Engineering Structures*, 184: 15-36.
Reddy, J. (1997). "On locking-free shear deformable beam finite elements." *Computer methods in applied mechanics and engineering*, 149(1-4): 113-132.
Remino, M., Trento, U. d. s. d. (2004). *Shear Modeling of Reinforced Concrete Structures*,
Ricles, J. M., Yang, Y.-S., Priestley, M. N. (1998). "Modeling nonductile R/C columns for seismic analysis of bridges." *Journal of Structural Engineering*, 124(4): 415-425.
Roh, H., Reinhorn, A. M., Lee, J. S. (2012). "Power spread plasticity model for inelastic analysis of reinforced concrete structures." *Engineering Structures*, 39: 148-161.
Saadé, K., Espion, B., Warzée, G. (2004). "Non-uniform torsional behavior and stability of thin-walled elastic beams with arbitrary cross sections." *Thin-walled structures*, 42(6): 857-881.
Salehi, M., Sideris, P. (2017). "Refined gradient inelastic flexibility-based formulation for members subjected to arbitrary loading." *Journal of Engineering Mechanics*, 143(9): 04017090.
Salehi, M., Sideris, P., Liel, A. (2017). "Seismic Collapse Analysis of RC Framed Structures using the Gradient Inelastic Force-Based Element Formulation." *16th World Conference on Earthquake Engineering (16WCEE)*, Santiago Chile, January 9 - 13,
Salehi, M., Sideris, P. (2018). "A Finite-Strain Gradient Inelastic Beam Theory and a Corresponding Force-Based Frame Element Formulation." *International Jounral for Numerical Methods in Engineering*, 116(6): 380-411, DOI: https://doi.org/10.1002/nme.5929.
Salehi, M., Sideris, P., Liel, A. (2020). "Assessing Damage and Collapse Capacity of Reinforced Concrete Structures Using the Gradient Inelastic Beam Element Formulation." *Engineering Structures Journal (In press)*.
Saritas, A., Filippou, F. C. (2009). "Inelastic axial-flexure–shear coupling in a mixed formulation beam finite element." *International Journal of Non-Linear Mechanics*, 44(8): 913-922.
Scott, M., Hamutçuoğlu, O. (2008). "Numerically consistent regularization of force ‐ based frame elements." *International journal for numerical methods in engineering*, 76(10): 1612-1631.
Scott, M. H., Fenves, G. L. (2006). "Plastic hinge integration methods for force-based beam–column elements." *Journal of Structural Engineering*, 132(2): 244-252.
Sezen, H., Chowdhury, T. (2009). "Hysteretic model for reinforced concrete columns including the effect of shear and axial load failure." *Journal of Structural Engineering*, 135(2): 139-146.
Sharifi, A., Banan, M. R., Banan, M. R. (2020). "A Macro-method for Including Bond–Slip Flexibility Within Fibre Element Formulation for Simulating Hysteretic Behaviour of RC Beam–Column Members." *Iranian Journal of Science and Technology, Transactions of Civil Engineering*: 1-13.
Sideris, P. (2012). *Seismic analysis and design of precast concrete segmental bridges*, State University of New York at Buffalo. ISBN 1267672692.

Sideris, P., Salehi, M. (2016). "A Gradient Inelastic Flexibility-Based Frame Element Formulation." *Journal of Engineering Mechanics*, 142(7): 04016039, DOI: doi:10.1061/(ASCE)EM.1943-7889.0001083.

Spacone, E., Ciampi, V., Filippou, F. (1996). "Mixed formulation of nonlinear beam finite element." *Computers & structures*, 58(1): 71-83.

Stramandinoli, R. S., La Rovere, H. L. (2012). "FE model for nonlinear analysis of reinforced concrete beams considering shear deformation." *Engineering structures*, 35: 244-253.

Valipour, H. R., Foster, S. J. (2009). "Nonlocal Damage Formulation for a Flexibility-Based Frame Element." *Journal of Structural Engineering*, 135(10): 1213-1221.

Vecchio, F., Shim, W. (2004). "Experimental and analytical reexamination of classic concrete beam tests." *Journal of Structural Engineering*, 130(3): 460-469.

Vecchio, F. J., Collins, M. P. (1986). "The modified compression-field theory for reinforced concrete elements subjected to shear." *ACI J.*, 83(2): 219-231.

Vecchio, F. J., Collins, M. P. (1988). "Predicting the response of reinforced concrete beams subjected to shear using modified compression field theory." *ACI Structural Journal*, 85(3): 258-268.

Wu, J. Y., Li, J., Faria, R. (2006). "An energy release rate-based plastic-damage model for concrete." *International journal of Solids and Structures*, 43(3-4): 583-612.

Xiao, Y., Priestley, M. N., Seible, F. (1993). *Steel jacket retrofit for enhancing shear strength of short rectangular reinforced concrete columns*, Department of Applied Mechanics & Engineering Sciences, University of California-San Diego, San Diego, Calif,

Xu, S.-Y., Zhang, J. (2012). "Axial–shear–flexure interaction hysteretic model for RC columns under combined actions." *Engineering Structures*, 34: 548-563.

Xu, S. Y., Zhang, J. (2011). "Hysteretic shear–flexure interaction model of reinforced concrete columns for seismic response assessment of bridges." *Earthquake Engineering & Structural Dynamics*, 40(3): 315-337.

Zeris, C. A., Mahin, S. A. (1988). "Analysis of reinforced concrete beam-columns under uniaxial excitation." *Journal of structural engineering*, 114(4): 804-820.

Zia, Y. B., Khan, A. A. "Comparison of various higher order shear deformation theories for static and modal analysis of composite beam." *Proc., IOP Conference Series: Materials Science and Engineering*, IOP Publishing, 012170.